Calcium-Promoted Interaction between the C2-Domain Protein EHB1 and Metal Transporter IRT1 Inhibits Arabidopsis Iron Acquisition[1]

Imran Khan,[a] Regina Gratz,[a,b] Polina Denezhkin,[b] Stephan N. Schott-Verdugo,[e,g] Kalina Angrand,[b] Lara Genders,[a] Rubek Merina Basgaran,[a] Claudia Fink-Straube,[c] Tzvetina Brumbarova,[a,b] Holger Gohlke,[e,f] Petra Bauer,[a,b,d] and Rumen Ivanov[a,b,2,3]

[a]Institute of Botany, Heinrich-Heine University, D-40225 Düsseldorf, Germany
[b]Former address: Department of Biosciences-Plant Biology, Saarland University, D-66123 Saarbrücken, Germany
[c]Leibniz Institute for New Materials, D-66123 Saarbrücken, Germany
[d]Cluster of Excellence on Plant Sciences, Heinrich-Heine University, D-40225 Düsseldorf, Germany
[e]Institute for Pharmaceutical and Medicinal Chemistry, Heinrich-Heine University, D-40225 Düsseldorf, Germany
[f]John von Neumann Institute for Computing, Jülich Supercomputing Centre & Institute of Complex Systems, ICS-6: Structural Biochemistry, Forschungszentrum Jülich GmbH, D-52425 Jülich, Germany
[g]Centro de Bioinformática y Simulación Molecular, Facultad de Ingeniería, Universidad de Talca, CL-3460000 Talca, Chile

ORCID IDs: 0000-0001-9692-5961 (I.K.); 0000-0002-8820-7211 (R.G.); 0000-0001-5828-1608 (P.D.); 0000-0003-0735-1404 (S.N.S.-V.); 0000-0002-3104-6795 (T.B.); 0000-0001-7909-4123 (R.I.).

Iron is a key transition element in the biosphere and is crucial for living organisms, although its cellular excess can be deleterious. Maintaining the balance of optimal iron availability in the model plant Arabidopsis (*Arabidopsis thaliana*) requires the precise operation of iron import through the principal iron transporter IRON-REGULATED TRANSPORTER1 (IRT1). Targeted inhibition of IRT1 can prevent oxidative stress, thus promoting plant survival. Here, we report the identification of an IRT1 inhibitor, namely the C2 domain-containing peripheral membrane protein ENHANCED BENDING1 (EHB1). EHB1 interacts with the cytoplasmically exposed variable region of IRT1, and we demonstrate that this interaction is greatly promoted by the presence of calcium. We found that EHB1 binds lipids characteristic of the plasma membrane, and the interaction between EHB1 and plant membranes is calcium-dependent. Molecular simulations showed that EHB1 membrane binding is a two-step process that precedes the interaction between EHB1 and IRT1. Genetic and physiological analyses indicated that EHB1 acts as a negative regulator of iron acquisition. The presence of EHB1 prevented the IRT1-mediated complementation of iron-deficient *fet3fet4* yeast (*Saccharomyces cerevisiae*). Our data suggest that EHB1 acts as a direct inhibitor of IRT1-mediated iron import into the cell. These findings represent a major step in understanding plant iron acquisition, a process that underlies the primary production of bioavailable iron for land ecosystems.

Deprived of the ability to escape unfavorable conditions, plants have developed powerful mechanisms for adapting to their environment (Haak et al., 2017). Nutrient availability in the soil can be a limiting factor for plant growth and plants respond to variations in nutrient concentrations by a variety of developmental and physiological responses (Giehl and von Wirén, 2014; Briat et al., 2015). Of particular importance is the acquisition of iron, an element abundant in the soil but poorly available to plants (Guerinot and Yi, 1994; Wedepohl, 1995). As a part of many key biological processes, iron is indispensable for life; however, in high doses it can cause deleterious effects and even death. Therefore, its controlled acquisition from the soil is essential for the plant. Arabidopsis (*Arabidopsis thaliana*) employs a reduction-based iron acquisition strategy (Römheld and Marschner, 1983; Brumbarova et al., 2015), in which actively-solubilized iron is first reduced by the FERRIC REDUCTASE-OXIDASE2 (FRO2; Robinson et al., 1999) and subsequently imported from the apoplastic space across the plasma membrane of the root epidermal cells by the bivalent metal transporter IRON-REGULATED TRANSPORTER1 (IRT1; Eide et al., 1996; Vert et al., 2002; Fourcroy et al., 2016).

The system is responsive to the amounts of available iron and is transcriptionally induced upon iron limitation (Brumbarova et al., 2015). Genes encoding IRT1 proteins are present throughout land plants and green algae, and show tight coregulation with the rest of the organism's iron acquisition and homeostasis machinery (Hanikenne et al., 2005; Ivanov et al., 2012a; Urzica et al., 2012; Ivanov and Bauer, 2017). In addition to this, the Arabidopsis IRT1 protein was shown to undergo posttranslational regulation involving covalent

modifications and regulated trafficking toward and away from the plasma membrane (Barberon et al., 2011, 2014; Shin et al., 2013; Ivanov et al., 2014; Dubeaux et al., 2018). Under iron deficiency, plasma membrane-localized IRT1 is modified by the E3 ubiquitin ligase IRT1-DEGRADATION FACTOR1 (IDF1), which leads to its clathrin-mediated endocytosis (Barberon et al., 2011, 2014; Shin et al., 2013). IRT1 was shown to sense the abundance of its noniron metal substrates zinc, manganese, and cobalt. When these are present in excess, IRT1 can bind them and recruit the CBL-INTERACTING PROTEIN KINASE 23 (CIPK23), which phosphorylates IRT1's variable region. Phosphorylated IRT1 is ubiquitinated by IDF1, internalized and degraded (Dubeaux et al., 2018). Internalized IRT1 can also be recycled and resent back to the plasma membrane. Two proteins, SORTING NEXIN1 (SNX1) and FYVE DOMAIN PROTEIN REQUIRED FOR ENDOSOMAL SORTING 1 (FREE1/FYVE1), have been implicated in this process (Barberon et al., 2014; Ivanov et al., 2014). In addition, FREE1/FYVE1 was shown to participate in the maintenance of the polar localization of IRT1 to the plasma membrane facing the rhizosphere (Barberon et al., 2014). A tight multilevel control of IRT1 activity counteracts uncontrolled iron acquisition that may otherwise overload the cellular capacity to safely store iron and result in extensive oxidative damage (Reyt et al., 2015; Le et al., 2016). Therefore, mechanisms that prevent the excessive entry of iron into the cell are essential to the survival of plants.

Members of the C2-domain abscisic acidrelated (CAR) protein family have recently emerged as key regulators of plant stress responses. These proteins share homology with the Arf GTPase activating protein family but lack the N-terminal Zn-finger motif, characteristic of the Arf GTPase activating protein family, and only contain a C2 calcium- and lipid-binding domain (Knauer et al., 2011). A characteristic feature of CAR proteins is a family-specific stretch of 48 amino acids inserted into the C2 domain that connects the two four-stranded beta sheets (Rodriguez et al., 2014). This domain, referred to as the "CAR signature domain," was shown to be involved in the protein–protein interaction between Arabidopsis CAR4, also named "AtGAP1," and the abscisic acid (ABA) receptors PYRABACTIN RESISTANCE 1 (PYR1)-LIKE1 (PYL1) and PYL6 (Rodriguez et al., 2014). Members of the CAR family have been characterized in rice (*Oryza sativa*) and Arabidopsis, and are involved in the responses to wounding, salinity, blue light and ABA, as well as in the root gravitropic response (Cheung et al., 2008, 2010, 2013; Knauer et al., 2011; Rodriguez et al., 2014). The Arabidopsis CAR-family member ENHANCED BENDING1 (EHB1), also known as "CAR6," was identified in a yeast two-hybrid screen as an interactor of the blue light response regulator NONPHOTOTROPIC HYPOCOTYL3. Physiological analysis revealed EHB1 as a negative regulator of blue light responses and further showed its involvement in root gravitropic responses (Knauer et al., 2011; Dümmer et al., 2016).

Our aim was to investigate the interactome of IRT1 for the identification of processes and molecular players involved in the regulation of IRT1 function. Using a yeast two-hybrid screen with IRT1's cytoplasmically exposed variable region, we identified EHB1 as an IRT1 protein interactor. EHB1 was able to bind a subset of phosphatidylinositide lipids. The EHB1-IRT1 and EHB1-lipid interactions were significantly promoted by the presence of calcium. Molecular simulations suggested that the membrane binding of EHB1 precedes the interaction between EHB1 and IRT1. Physiological analysis showed that EHB1 presence negatively affects the import of apoplastic iron into the root and that EHB1 directly affects IRT1-dependent iron acquisition. The data suggest a role of EHB1 in mediating calcium signals for the inhibition of iron acquisition.

RESULTS

IRT1 Interacts with EHB1

To identify proteins involved in the regulation of iron import from the rhizosphere, we looked for interactors of IRT1. We used the cytoplasmically exposed variable region of IRT1 (referred to as "IRT1vr," residues 145–192), as it constitutes the key IRT1 scaffold for regulatory and modification inputs. IRT1vr was used as bait in a yeast two-hybrid screen against an expression library prepared from complementary DNA (cDNA) of iron-deficient Arabidopsis roots. Among the colonies growing on the selection medium, IRT1vr together with the C2 domain-containing protein EHB1 were found in 34% of the cases. EHB1 is a part of a 10-member protein family; however, none of the other members were identified in the screen. UBIQUITIN 10, a previously reported IRT1 interactor (Barberon et al., 2011), was also identified in this screen. We could verify the interaction in a targeted yeast two-hybrid assay using a recloned full-length EHB1 (Fig. 1A). In this case, only

[1]This work was supported by the Deutsche Forschungsgemeinschaft (DFG, German Research Foundation Project no. 267205415–SFB 1208 and projects A03 to H.G. and B05 to P.B.); German Academic Exchange Service (DAAD grant no. 91541023 to I.K.); Saarland University (61cl/Anschub2012/ivanov to R.I.); and Heinrich Heine University (SFF-F 2014/730-15 Ivanov to R.I.).

[2]Author for contact: rumen.ivanov@uni-duesseldorf.de.

[3]Senior author.

The author responsible for distribution of materials integral to the findings presented in this article in accordance with the policy described in the Instructions for Authors (www.plantphysiol.org) is: Rumen Ivanov (rumen.ivanov@uni-duesseldorf.de).

R.I. and P.B. designed the research; R.I. designed experiments; H.G. and S.N.S.-V. designed computations; I.K., R.G., P.D., S.N.S.-V., K.A., L.G., R.M.B., C.F.-S., T.B., and R.I. performed research; T.B., R.G., P.B., H.G., S.N.S.-V., and R.I. analyzed data; R.I. wrote the article with contributions by S.N.S.-V. and H.G.; R.G., T.B., P.B., and R.I. commented and corrected the article; H.G., P.B., and R.I. acquired funding.

www.plantphysiol.org/cgi/doi/10.1104/pp.19.00163

the IRT1vr-EHB1 combination but none of the negative control cotransformations produced colonies on the triple selection medium, suggesting a specific interaction between IRT1vr and EHB1. The known SNX1 homodimerization (Pourcher et al., 2010) was used as a positive control (Fig. 1A). To verify the interaction further, we used the two fragments, together with several deletion versions, for an interaction test in plant cells using bimolecular fluorescence complementation (BiFC; Fig. 1, B and L; Grefen and Blatt, 2012). A positive BiFC signal indicated the IRT1vr-EHB1 interaction in this system (Fig. 1, C–E). The CAR signature domain was found to be the protein interaction interface for the EHB1 homolog CAR4 interaction with PYR/PYL receptors (Rodriguez et al., 2014). EHB1 protein lacking the CAR signature domain was not able to interact with IRT1vr in transformed cells (Fig. 1, F–H). On the other hand, the signature domain alone was sufficient for an interaction with IRT1vr (Fig. 1, I–K), suggesting that this domain mediates the interaction on the side of EHB1. To delimit the protein interaction on the side of IRT1vr, we created four different deletion constructs of IRT1vr that contained or were devoid of the previously described regulatory residues for metal binding, phosphorylation, and ubiquitination, taking into account the predicted secondary structure (Fig. 1L; Ivanov and Bauer, 2017). EHB1 was able to bind three IRT1vr fragments (Fig. 1, M–R and V–X) but not IRT1vrΔ3 (Fig. 1, S–U), which lacks the predicted helical regions in proximity to transmembrane domains III and IV (Ivanov and Bauer, 2017). These data show that the interaction requires the part of IRT1vr flanking the transmembrane regions and the CAR signature domain of EHB1. The involvement of the EHB1 CAR signature domain in protein–protein interaction is thus consistent with previous reports (Rodriguez et al., 2014).

IRT1 Interaction with EHB1 Is Calcium-Dependent

Because EHB1 was able to bind to the cytoplasmically exposed variable region of IRT1, we tested its ability to interact with the full-length IRT1 protein in plant cells. For this, we expressed EHB1-HA and IRT1-GFP fusions and performed coimmunoprecipitation. The presence of EHB1-HA in the IRT1-GFP–containing sample was visible after anti-GFP immunoprecipitation (Fig. 2A), suggesting that the full-length proteins can form a complex. EHB1-HA was present as a double band, one at the expected size of 25 kD and another of ~35 kD, presumably representing a modified form of the protein. As EHB1 is a calcium-dependent protein due to the presence of a C2 domain, we hypothesized that calcium concentration might influence EHB1's capacity to bind IRT1. When the coimmunoprecipitation procedure was performed in the presence of 100-μM Ca^{2+}, we observed a dramatic increase of recovered EHB1-HA (Fig. 2B). The EHB1 protein lacking the CAR signature domain was not able to interact with the full-length IRT1-GFP, irrespective of the calcium availability (Fig. 2, C and D). This confirms the importance of the CAR signature domain for the formation of the IRT1-EHB1 complex and shows that the strength of the interaction is dependent on the local calcium concentration.

EHB1 and IRT1 Colocalize at the Plasma Membrane

C2 domain proteins are described as peripheral membrane proteins and previous studies have suggested that CAR-family proteins localize partially at the plasma membrane (Cheung et al., 2010; Demir et al., 2013; Rodriguez et al., 2014). We expected that as an IRT1 interactor, EHB1 should also localize to the membrane system of plant cells. An EHB1-GFP fusion protein expressed in *Nicotiana benthamiana* epidermis cells resulted in a broad localization pattern with signals visible also in the nucleus (Fig. 2, E–G). We performed a control immunoblot, which revealed two bands, one with the expected size of 57 kD and one at 67 kD (Fig. 2H), likely corresponding to a modified EHB1-GFP form, as observed with EHB1-HA. No signal was observed in the 27-kD region that would suggest the existence of free GFP. We first investigated the colocalization of free GFP and the plasma membrane marker AHA1-mRFP (Caesar et al., 2011). Distinct, spatially-separated signals were visible in cells coexpressing the two proteins, suggesting that they differ in their subcellular localization (Fig. 2, I–K). This was confirmed by intensity-based colocalization scatterplot (Fig. 2L), and by plasmolyzing the cells in the presence of mannitol. After plasmolysis, AHA1-mRFP was seen in Hechtian strands, by which the plasma membrane remains attached to the cell wall, whereas GFP was absent from these structures (Fig. 2, M–O). Next, we tested the EHB1-GFP plasma membrane localization. In the cell periphery, it displayed a good colocalization with the AHA1-mRFP marker. We could observe additional EHB1-GFP intracellular signals, not visible for AHA1-mRFP (Fig. 2, P–R). This demonstrates the partial presence of EHB1 at the plasma membrane in plant cells. Intensity-based colocalization scatterplot confirmed the observation (Fig. 2S). Upon mannitol-induced plasmolysis, we found both EHB1-GFP and the AHA1-mRFP marker in Hechtian strands (Fig. 2, T–V), confirming the presence of EHB1-GFP at the plasma membrane. We then performed a colocalization analysis between EHB1-GFP and IRT1-mCherry. Signals at the cell periphery showed a high degree of colocalization (Fig. 2, W–Z). Together, the data suggest that EHB1 is partially localized at the plasma membrane where it colocalizes with IRT1.

EHB1 Can Bind Phosphoinositides

To understand whether lipids are targeted by EHB1, we expressed and purified recombinant StrepII-tagged EHB1 in *Escherichia coli* (Supplemental Fig. S1) to use in a lipid overlay assay. Probing a set of immobilized

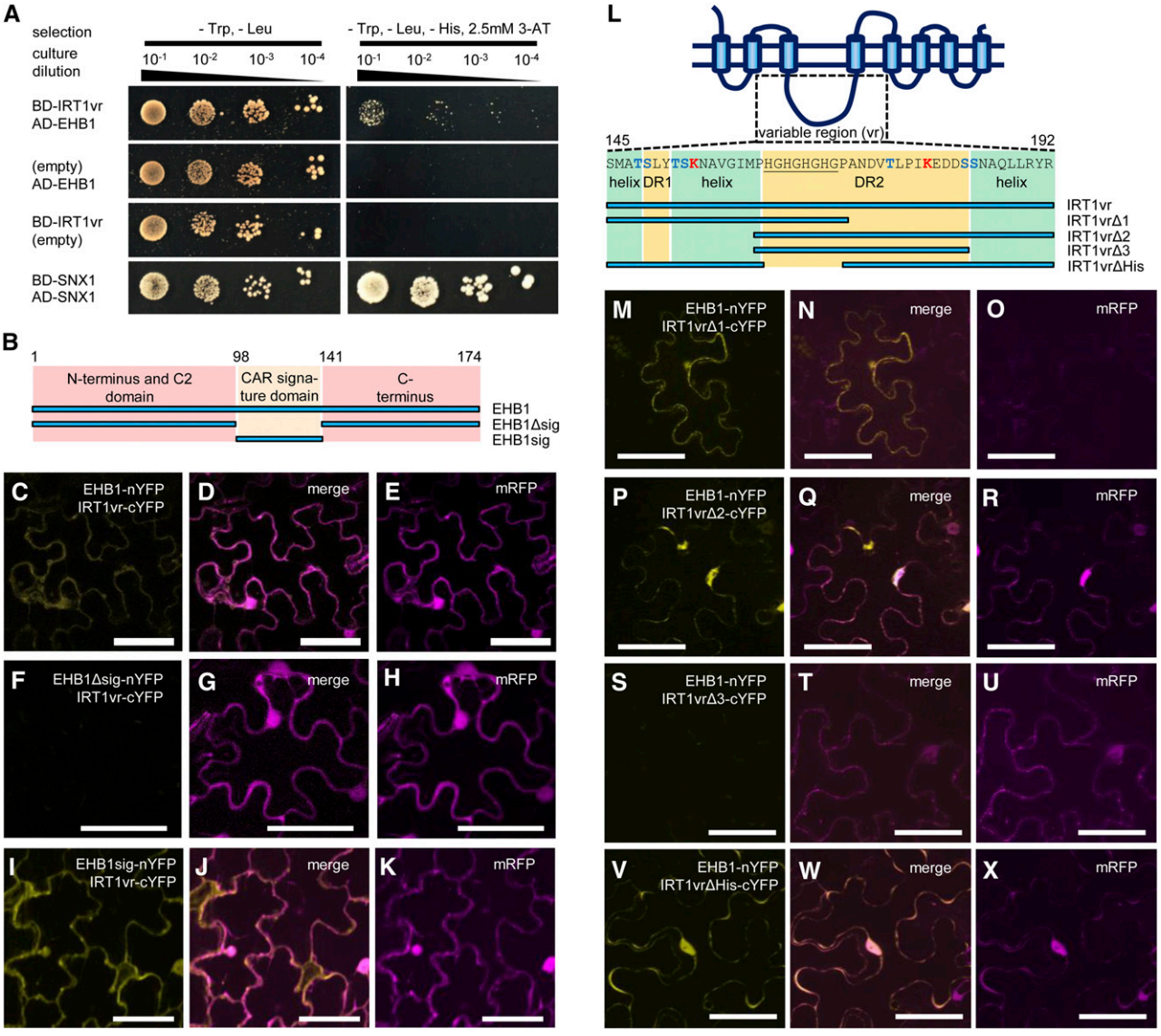

Figure 1. EHB1 interacts with the variable region of IRT1. A, Targeted yeast two-hybrid assay, showing the interaction between BD-IRT1vr (IRT1 variable region) and AD-EHB1. Growth on triple selection medium (right) indicates protein–protein interaction. B, Schematic representation of EHB1 protein and the two fragments used in the BiFC experiments testing interaction with IRT1vr. The position of the CAR signature domain, as defined in Rodriguez et al. (2014), together with the amino acid numbers, are indicated. C to K, Targeted BiFC experiment for verification of the interaction between EHB1 and its fragments (depicted in B) with the IRT1vr. Signal in the YFP channel indicates a reconstitution of a functional YFP protein as a consequence of an interaction. Signal in the RFP channel is used as a control, showing that the cell was transformed. Each of the shown protein combinations was tested a minimum of three times yielding comparable results. Bars = 50 μm. L, Schematic representation of the IRT1vr and the IRT1vr-derived fragments used in the BiFC experiments testing interaction with EHB1. The different predicted secondary structures within IRT1vr, as defined in Ivanov and Bauer (2017), are indicated. DR1 and DR2 indicate the predicted disordered regions. The two Lys residues, known as ubiquitination targets, are labeled in red. The known potential phosphorylation targets directing the interaction with IDF1 E3 ubiquitin-ligase are shown in blue. The His-rich region, characteristic for the variable region of the ZIP-family transporters and involved in metal binding, is underlined. Numbers indicate the first and last amino acid of IRT1vr within IRT1 protein. M to X, Targeted BiFC experiment for verification of the interaction between the IRT1vr and its fragments (depicted in L) with EHB1. Signal in the YFP channel indicates a reconstitution of a functional YFP protein as a consequence of an interaction. Signal in the RFP channel is used as a control, showing that the cell was transformed. Each of the shown protein combinations was tested a minimum of three times yielding comparable results. Bars = 50 μm.

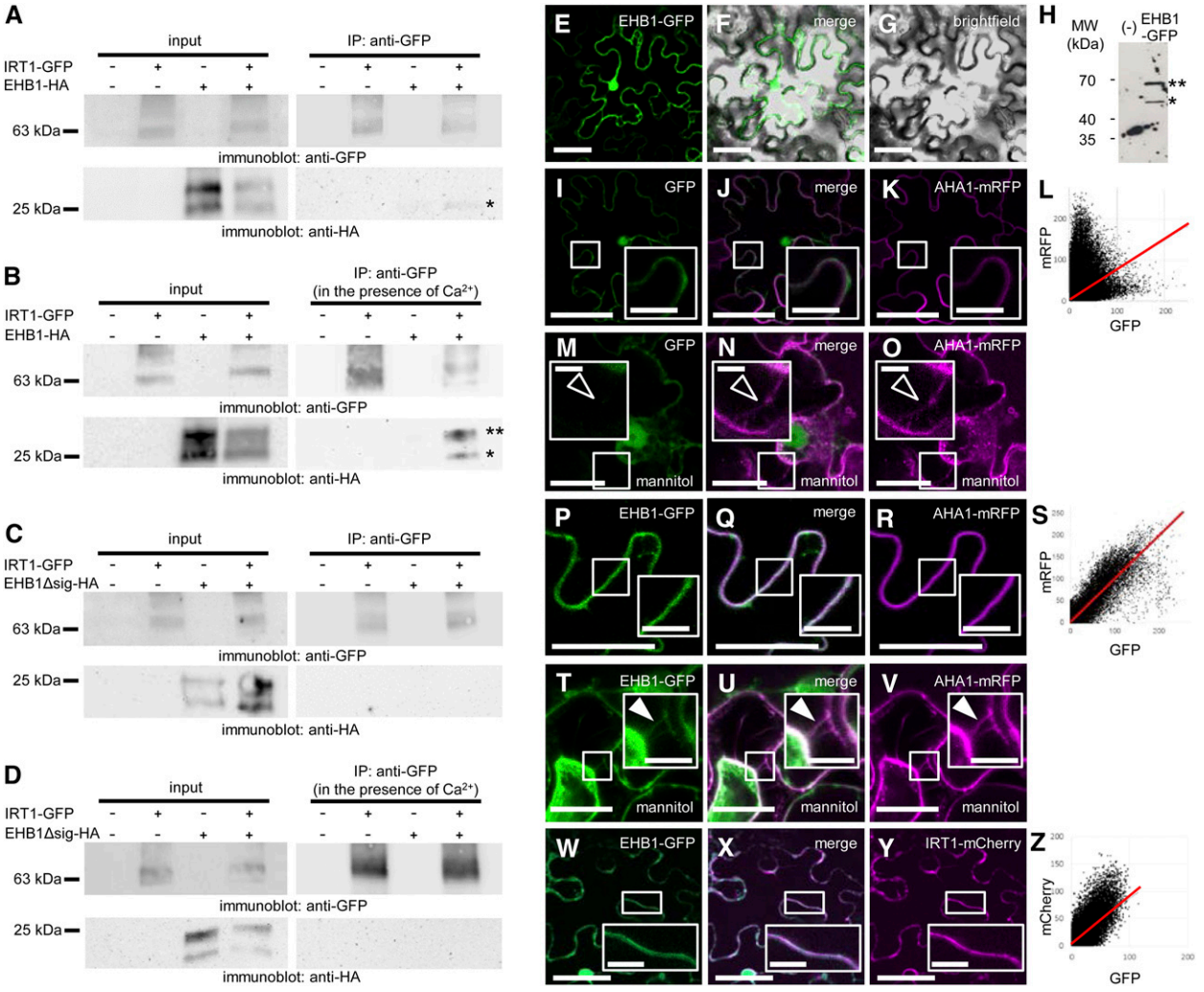

Figure 2. Interaction and subcellular localization of full-length IRT1 and EHB1. A, EHB1-HA coimmunoprecipitates with IRT1-GFP. IRT1-GFP, EHB1-HA or a combination of the two were expressed in *N. benthamiana* epidermis cells and used for anti-GFP immunoprecipitation. The samples before (left, input) and after (right, IP: anti-GFP) the procedure were tested by immunoblot analysis. Weak, yet specific, presence of EHB1-HA was found in the combined immunoprecipitated sample. Nontransformed samples were used as controls. The experiment was performed three times yielding comparable results. Asterisk indicates coimmunoprecipitated EHB1-HA. B, The same experiment as in (A) was performed in the presence of 100-μM Ca^{2+}. A marked increase of EHB1-HA signal in the combined sample could be observed, in comparison to (A). The experiment was performed three times yielding comparable results. Asterisks indicate coimmunoprecipitated EHB1-HA forms. C, EHB1Δsig-HA fails to coimmunoprecipitate with IRT1-GFP. IRT1-GFP, EHB1Δsig-HA, or a combination of the two was expressed in *N. benthamiana* epidermis cells and used for anti-GFP immunoprecipitation. The samples before (left, input) and after (right, IP: anti-GFP) the procedure were tested by immunoblot. No EHB1-HA signals could be detected in the combined immunoprecipitated sample. Nontransformed samples were used as controls. The experiment was performed three times yielding comparable results. D, The same experiment as in (C) was performed in the presence of 100-μM Ca^{2+}. No EHB1-HA signals could be detected in the combined immunoprecipitated sample. The experiment was performed three times yielding comparable results. E to G, Localization of EHB1-GFP in *N. benthamiana* epidermis cells. H, Anti-GFP immunoblot made on extracts either expressing or not EHB1-GFP. No obvious degradation products or free GFP can be seen. The single asterisk indicates the EHB1-GFP band at the predicted 57 kD and the double asterisk—an additional band at 67 kD. I to L, Colocalization between free GFP and ARABIDOPSIS H^+-ATPASE 1 (AHA1)-monomeric Red Fluorescent Protein (mRFP). L, Scatterplot of the signals in the GFP and mRFP channels, showing the typical distribution of non-colocalizing signals. M–O, Colocalization between free GFP and AHA1-mRFP in mannitol-plasmolyzed cells. Open arrowheads point toward Hechtian strands indicating the presence of AHA1-mRFP at the plasma membrane. Free GFP could not be found in these structures. P–S, Colocalization between EHB1-GFP and AHA1-mRFP in the region of the plasma membrane. S, Represents a scatterplot of the signals in the GFP and mRFP channels, showing the typical distribution of colocalizing signals. T to V, Colocalization between EHB1-GFP and AHA1-mRFP in mannitol-plasmolyzed cells. Solid arrowheads point toward Hechtian strands indicating the presence of AHA1-mRFP at the plasma membrane. EHB1-GFP was also present in these structures, indicating its localization at the plasma membrane. W–Z, Colocalization between EHB1-GFP and

lipids on the Membrane Lipid Strip (Echelon) showed a strong preference of the purified StrepII-EHB1 protein for phosphatidylinositol (PtdIns) and phosphatidylinositol 4-phosphate (PtdIns4P; Fig. 3A). The finding is particularly intriguing because PtdIns4P is known to accumulate in the plasma membrane of plant cells and has emerged as a key target for the attachment of regulatory proteins (Simon et al., 2016). To verify the finding in an actual membrane environment, we generated liposomes with phosphatidylcholine (PC) as the base lipid. After an incubation with StrepII-EHB1, we pelleted the liposomes by centrifugation. We then monitored the presence of StrepII-EHB1 in the pellet and the supernatant by protein immunoblot followed by band intensity quantification (Fig. 3, B and C). StrepII-EHB1 was copelleted with liposomes containing PC-PtdIns and PC-PtdIns4P mixture, indicating that the protein was able to bind the liposome surface. No signal could be detected in the pelleted fraction of liposomes containing exclusively PC, showing that StrepII-EHB1 bound specifically PtdIns and PtdIns4P lipids. Nor was there signal in the pellet fraction in the absence of liposomes, which demonstrates the absence of protein aggregation (Fig. 3B). Interestingly, when the experiment was performed in the presence of 100-μM Ca^{2+}, a relative enrichment of the membrane-bound StrepII-EHB1 could be observed, especially in the case of PtdIns-containing liposomes (Fig. 3, B and C). The liposome binding activity of EHB1 was unchanged when the signature domain was deleted (Supplemental Fig. S2A). This shows that the signature domain does not affect the membrane-binding capacity of EHB1, and this finding is in agreement with the described structure of the CAR proteins (Rodriguez et al., 2014). Taken together, EHB1 can bind PtdIns and PtdIns4P-containing membranes and the binding is partially enhanced in the presence of calcium.

EHB1 Membrane Association Is Calcium-Dependent

To further understand the significance of calcium for EHB1 membrane association, we generated an Arabidopsis line expressing an HA-EHB1 fusion (Supplemental Figs. S3 and S4B). Using this, we performed ultracentrifugation-based separation of root membrane and soluble fractions (Fig. 3D; Supplemental Fig. S2B). Plants were grown in the two-week growth system under sufficient iron and iron-deficient conditions to account for potential changes in membrane composition under these two growth regimes. In the absence of added calcium, no significant presence of the HA-EHB1 protein could be observed in microsomal fractions. The presence of 100-μM Ca^{2+}, however, resulted in a marked increase of membrane-bound HA-EHB1. The effect was observed and was comparable in both standard-grown and iron-deficient plant samples (Fig. 3D; Supplemental Fig. S2B). This shows that the presence of calcium is an important prerequisite for EHB1 binding to plant membranes. Stimulus-driven relocalization of CAR family proteins to the plasma membrane has been observed in the case of the rice OsGAP1 (Cheung et al., 2010). Our data suggest that the process of EHB1 membrane association might be calcium-driven. At the same time the data show that iron starvation likely does not dramatically affect the availability of EHB1 binding sites in plant membranes.

Molecular Dynamics Simulations Suggest a Two-Step Binding Mode of EHB1 at the Membrane

To obtain a model of the binding of EHB1 at the plasma membrane at the atomistic level, a homology model of EHB1 was generated based on the structures of the homologous proteins CAR1 and CAR4. Molecular dynamics (MD) simulations of EHB1 binding were performed in an explicit solvent/membrane environment. The EHB1 model contained two calcium ions in the calcium binding site, as indicated by structures of CAR homologs (Diaz et al., 2016). The membrane bilayer was composed of a 4:4:1 ratio of 1,2-dioleoyl-SN-glycero-3-phosphocholine:1,2-dioleoyl-SN-glycero-3-phosphoethanolamine:1,2-dioleoyl-SN-glycero-3-phosphoglycerol (DOPC/DOPE/DOPG), resembling the composition of a plant plasma membrane (Furt et al., 2011). To avoid any bias, in the starting configuration of the system, EHB1 was placed ~25 Å apart from the closest membrane surface. During the MD simulations, EHB1 was then allowed to diffuse freely. In all of the five independent replica simulations performed, after ~1 μs of simulation time, EHB1 bound to the membrane via the calcium binding site (Fig. 3, E and F; Supplemental Movie). Furthermore, four out of five replicas showed a potassium ion in the close vicinity of the calcium binding site, similar to the homolog Protein Kinase C-α (PKC-α; Fig. 3F; Guerrero-Valero et al., 2009). Finally, EHB1 showed a strong tendency to tilt and to engage in interactions with the membrane with its sides, as demonstrated by a tilt angle close to 90° with respect to the membrane normal. In one replica, the protein interacted that way during almost the complete simulation time (Fig. 3, G and H). Interestingly, the interaction does not occur via a site described as the polybasic patch in homologs (Li et al., 2006), but rather through residues 51–62, 140–142, and 164–168. In the tilted configuration, the CAR-signature domain and the polybasic patch remain close to the surface (Fig. 3H). We noted that the composition of amino acids within the polybasic patch, putatively interacting with phosphoinositides, differs between PKC-α and EHB1, as well as between EHB1

Figure 2. (*Continued.*)
IRT1-mCherry in the region of the plasma membrane. Z, Scatterplot of the signals in the GFP and mCherry channels showing the typical distribution of colocalizing signals. Bars = 20 μm; bars in insets = 5 μm.

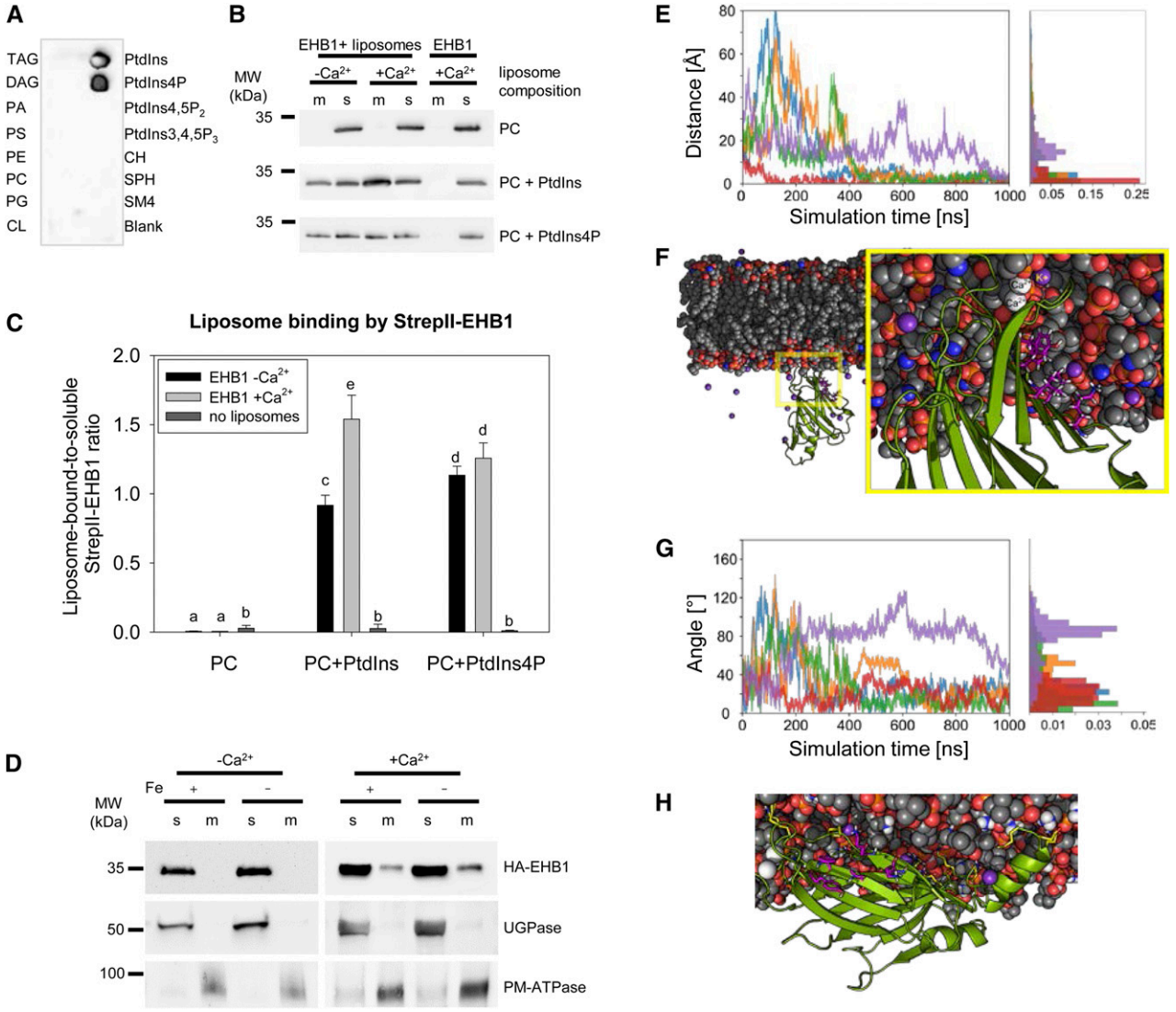

Figure 3. EHB1 binds membranes. A, Lipid overlay assay using StrepII-EHB1. Black signal shows the zones of the strip where StrepII-EHB1 was retained after washing. The experiment was performed three times yielding comparable results. TAG, triacylglycerol; DAG, diacylglycerol; PA, phosphatidic acid; PS, phosphatidyl-Ser; PE, phosphatidylethanolamine; PG, phosphatidylglycerol; CL, cardiolipin; CH, cholesterol; SPH, sphingomyelin; SM4, 3-O-sulfogalactosylceramide. B, Binding of StrepII-EHB1 to membrane lipids. Liposomes containing PC were used as controls. After incubation with StrepII-EHB1, the liposomes were pelleted and the membrane (m), and soluble (s) fractions analyzed by immunoblot. Presence of StrepII-EHB1 in the membrane fraction indicates liposome binding. The experiment was performed three times yielding comparable results. MW, molecular weight. C, Quantification of data presented in (B). Error bars represent SD, $n = 3$. Letters above the bars indicate statistically significant difference ($P < 0.05$). D, Extracts from HA-EHB1-expressing Arabidopsis plants were fractionated into microsomal (m) and soluble (s) fraction in either the absence ($-Ca^{2+}$) or presence ($+Ca^{2+}$) of calcium. The composition of the fractions was analyzed using immunoblots. The soluble enzyme UDP-Glc pyrophosphorylase (UGPase) and the plasma membrane H^+-ATPase (PM-ATPase) were used as markers. The experiment was performed three times yielding comparable results. E–H, EHB1 membrane interactions through the calcium binding site based on five independent MD simulations of 1-μs length in the presence of a membrane bilayer with a 4:4:1 ratio of DOPC/DOPE/DOPG. E, Distance between the calcium ions bound to the protein and the center of mass of the phosphorous atoms of the phospholipids of the closest leaflet over the simulation time; in the starting configuration, EHB1 was placed ~25 Å away from the membrane surface. In all replicas, EHB1 binds to the membrane surface through the calcium binding site. F, Representative structure showing an EHB1 configuration (green) bound to the membrane (gray carbon atoms) through the calcium binding site (Ca^{2+}: white spheres). An additional potassium ion was found to bind to an extra calcium binding site (magenta). G, Tilt angle defined between the vector formed by the center of mass of EHB1 with the complexed calcium ions and the membrane normal over the simulation time. A repeated, frequent, and, in one case, persistent tilting of EHB1 was observed in the replica simulations. H, Representative structure of the "parallel" configuration of EHB1 at the membrane. Residues that show direct interactions with the membrane are colored yellow; residues that correspond to the described polybasic patch are colored magenta.

and other CAR-family members (Supplemental Fig. S2, C–F). In PKC-α, these amino acids can interact with all P groups of PtdIns4,5P_2, whereas this is not possible for EHB1. Thus, the different amino acid composition in the case of EHB1 might contribute to the observed changes in lipid-binding specificity (Supplemental Fig. S2, C–F). To conclude, under the chosen simulation conditions, EHB1 shows a clear trend to bind to the membrane via the calcium binding site and then to tilt toward the membrane.

EHB1 Acts as a Negative Regulator of Iron Acquisition

CAR proteins that bind to signaling protein intermediates like the ABA receptor and NONPHOTOTROPIC HYPOCOTYL3 affect the physiological responses to ABA and blue light in a significant manner (Knauer et al., 2011; Rodriguez et al., 2014). Our next aim was to understand whether the interaction between IRT1 and EHB1 also affects downstream physiological reactions, in this case the plant capacity to acquire iron. To estimate the role of EHB1 in iron acquisition, we first analyzed two mutants carrying *EHB1* loss-of-function alleles, *ehb1-1* and *ehb1-2*, for which we confirmed the absence of full-length *EHB1* transcript, and two HA-EHB1 overexpressing lines (Supplemental Fig. S4). Control Col-0 wild-type, *ehb1*, and HA-EHB1 plants were grown in the 2-week growth system. Under iron-deficient conditions, wild-type as well as HA-EHB1-expressing plants developed the characteristic iron-deficiency chlorosis, whereas the effect was much less pronounced in the two *ehb1* lines (Fig. 4A). Leaf chlorosis is caused by a decrease in the chlorophyll content. Chlorophyll content in all plant lines was lower under iron-deficient than that under iron-sufficient conditions. However, in agreement with the morphological observations, the chlorophyll content was lowest in the HA-EHB1 lines, whereas it was similar in *ehb1* mutant lines under iron deficiency compared with that in wild type grown with sufficient iron. This shows that, compared to wild-type plants, *ehb1* mutant plants are less sensitive whereas HA-EHB1 lines are more sensitive to iron deficiency (Fig. 4B). As a key readout for the efficiency of the reduction-based iron acquisition system, we measured the activity of the FRO2 protein, functioning as the principal root-surface ferric reductase, the step before uptake of ferrous iron by IRT1 (Fig. 4C). As expected, the activity was strongly increased under iron deficiency in all tested genotypes. The absence of EHB1, however, led to a significant increase of FRO2 activity under iron deficiency in comparison to that in the wild type. Conversely, HA-EHB1 lines showed a reduced activity under these conditions compared to that in both wild-type and *ehb1* plants (Fig. 4C). The result is consistent with the phenotypical observations and shows that, in the absence of EHB1, the iron acquisition system is more active. This suggests that EHB1 might function as a negative regulator of iron acquisition. We then examined the expression level of the *EHB1* gene in response to iron availability (Fig. 4D). In wild-type plants, we observed *EHB1* expression downregulation under iron deficiency compared to that under iron-sufficient conditions. In *ehb1* mutant plants, the *EHB1* expression levels were very low, whereas in HA-EHB1 overexpressing plants, the expression levels were

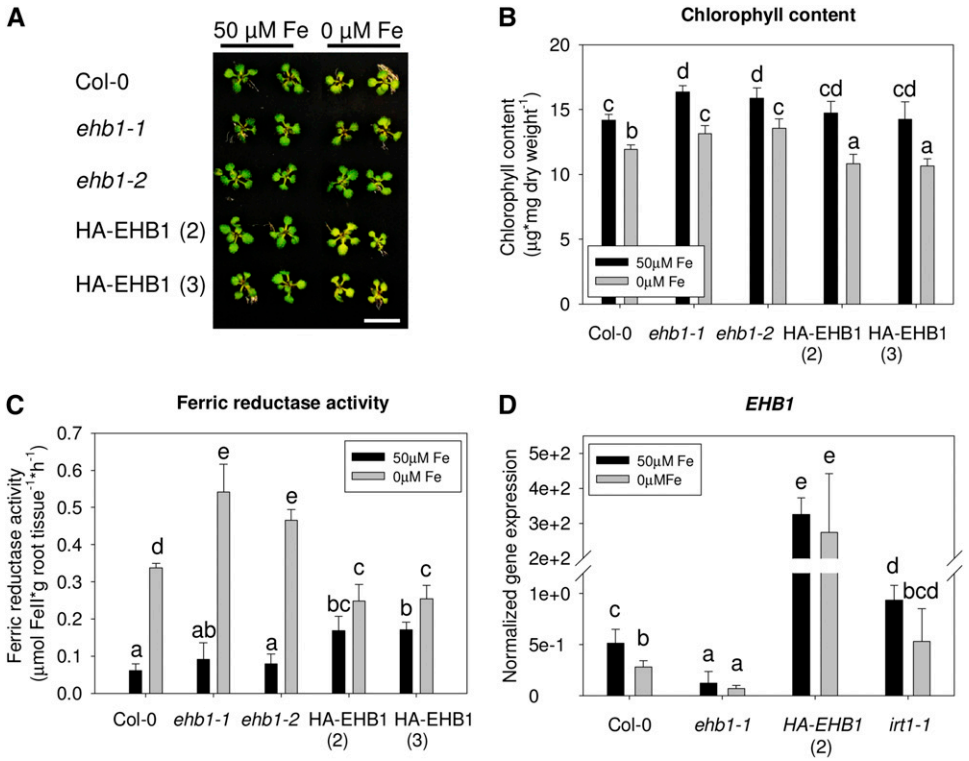

Figure 4. EHB1 inhibits Arabidopsis iron acquisition. A, Seedlings grown in the two-week growth system show iron deficiency chlorosis (leaf yellowing). In EHB1 loss-of-function plants, the effect is much less pronounced, compared to that in the wild-type (Col-0), whereas the effect is stronger in HA-EHB1-expressors. Bar = 1 cm. B, Total chlorophyll content of plants grown as in (A; $n = 5$). C, Ferric reductase activity of plants grown as in (A; $n = 5$). D, Expression level of *EHB1* under different iron regimes and in plants with modified iron acquisition capacity ($n = 3$). Error bars = SD. Letters above the bars indicate statistically significant difference ($P < 0.05$).

high and not affected by the iron status of the plant (Fig. 4D; Supplemental Fig. S5). In *IRT1* loss-of-function plants, *EHB1* expression levels were higher than that in the wild type under the corresponding conditions (Fig. 4D). This suggests that *EHB1* gene expression is influenced not only by the iron status of the plant but it also responds to the presence of IRT1. The observed downregulation under iron deficiency is consistent with its proposed role as a negative regulator.

We further investigated the role of EHB1 in root responses to iron deficiency by evaluating the expression of key iron-deficiency marker genes (Fig. 5; Supplemental Fig. S5). The *FERRITIN1* (*FER1*) gene responds positively to the amounts of iron present in the plant (Reyt et al., 2015) and it showed downregulation under iron deficiency in wild-type plants. In *ehb1* loss-of-function plants, *FER1* expression under sufficient iron supply was higher than that in the wild type, suggesting that higher amounts of iron are present in the root in the absence of EHB1. Consistently, the opposite effect, reduced *FER1* expression compared to that in wild-type plants under sufficient iron, was observed in HA-EHB1 plants and *irt1* mutant plants, the latter lacking the iron transporter (Fig. 5A). The expression of the FER-LIKE IRON DEFICIENCY-INDUCED TRANSCRIPTION FACTOR (*FIT*) gene was upregulated in response to iron deficiency compared to that under iron-sufficient conditions in wild-type, *ehb1* mutants, and HA-EHB1 plants (Fig. 5B; Supplemental Fig. S5). A marked upregulation of *FIT* under both iron conditions compared to that in the wild type could be observed in *IRT1* loss-of-function plants (Fig. 5B). The *FRO2* gene showed a stronger upregulation under iron deficiency in *ehb1* mutant plants and tendency for reduced upregulation in HA-EHB1 compared to that in the wild type (Fig. 5C; Supplemental Fig. S5). This effect was consistent with the measured ferric reductase activity in these plants. The *FRO2* expression pattern in *irt1* mutants was similar to that in *ehb1-1* (Fig. 5C). Surprisingly, the induction of the *IRT1* gene was less pronounced under iron deficiency in *ehb1* mutant plants than that in the wild type (Fig. 5D; Supplemental Fig. S5). The effect was consistent, as HA-EHB1 plants showed increased *IRT1* expression in the absence of iron compared to that in the wild type (Fig. 5D). *FRO2* and *IRT1* genes are both FIT transcriptional targets, although their induction levels are not strictly coupled and may vary significantly (Liberman et al., 2015; Wang et al., 2018). In addition, the documented broad stress-responsiveness of *IRT1* (Brumbarova et al., 2015), together with its expression and iron regulation in the absence of FIT (Barberon et al., 2011), suggests that additional transcriptional regulators may modulate its transcript levels. To test whether this effect somehow reflects the IRT1 protein abundance, we quantified the amount of IRT1 in total protein extracts of EHB1 loss-of-function plants. Compared to that in the wild type, roots of *ehb1* mutants were found to contain significantly more IRT1 protein (Fig. 5, E and F). This suggests that the absence of EHB1 leads to stabilization of IRT1 and the observed reduced gene expression in *ehb1* might be a compensatory mechanism for maintaining proper IRT1 levels.

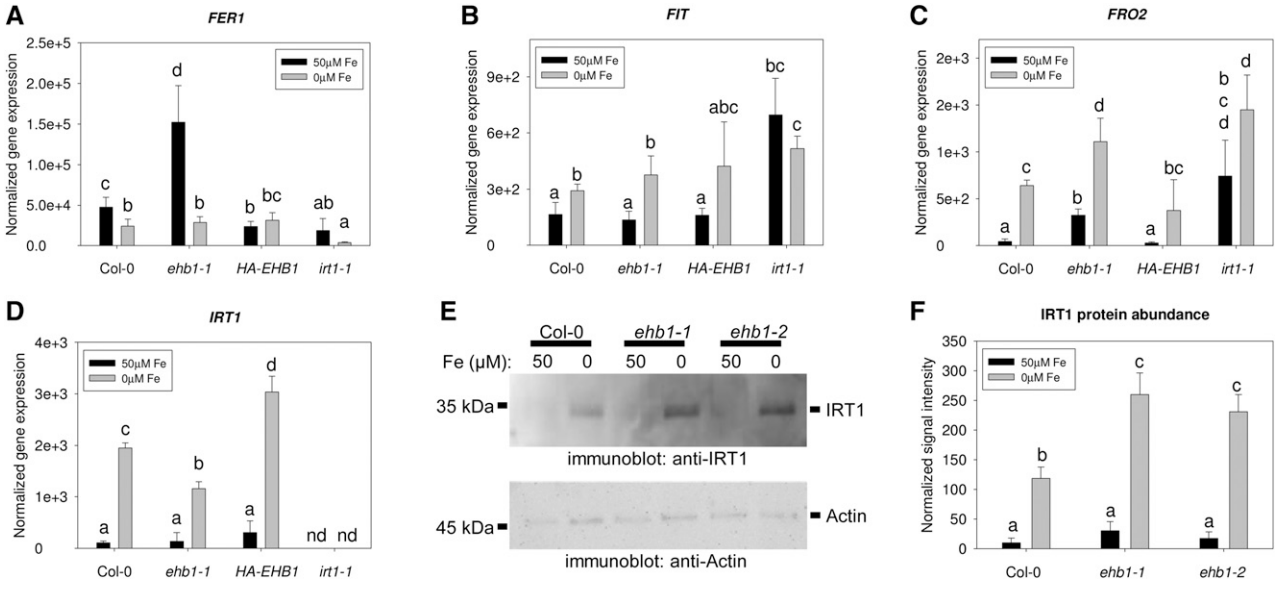

Figure 5. Regulation of iron homeostasis-related genes and proteins is affected by the absence of EHB1. A–D, Expression of genes related to iron storage (*FER1*, A) and acquisition (*FIT*, *FRO2*, and *IRT1*; B–D, respectively). Wild-type (Col-0) seedlings as well as one *ehb1* mutant and one HA-EHB1-expressing line were grown in the 2-week growth system. nd, not detected. Error bars = SD. Different letters above the bars indicate statistically significant difference ($P < 0.05$), $n = 3$. E, Anti-IRT1 immunoblot on extracts of plants grown in the 2-week growth system. Detection of actin was used as a loading control. The experiment was performed three times yielding comparable results. F, Quantification of the experiments presented in (E). Error bars = SD. Different letters above the bars indicate statistically significant difference ($P < 0.05$), $n = 3$.

Presence of EHB1 Suppresses Iron Assimilation

Modulation of IRT1 activity was shown to affect the extent at which iron, found in the root apoplast, is taken up by the plant (Ivanov et al., 2014). Because EHB1 affects IRT1 protein, we suspected that iron uptake is modulated in *ehb1* mutants and that this can be visualized at the level of apoplastic iron. We performed Perls-3,3′-diaminobenzidine tetrahydrochloride staining to visualize the apoplastic iron. Roots of wild-type plants, grown for 8 d under standard iron supply, showed moderate staining at the base of the root (Fig. 6, A and B), which decreased in the early differentiation zone (Fig. 6, A and C). On the other hand, the roots of the *fit-3* mutant, which fails to express *IRT1*, showed intensive iron staining (Fig. 6, M–O), as previously described for *IRT1* loss-of-function plants (Ivanov et al., 2014). Roots of *ehb1* mutant plants showed strongly decreased iron staining in comparison to that in the wild-type (Fig. 6, D–I), whereas HA-EHB1 plants showed enhanced staining in the early differentiation zone, compared to that in the wild-type (Fig. 6, J–L). These results are consistent with the observations on the physiology of EHB1 loss- and gain-of-function plants, and show that EHB1 affects the import of apoplastic iron, a process mediated by IRT1.

We evaluated how the observed alterations in iron import affect the metal contents in the seeds of soil-grown EHB1 loss- and gain-of-function plants. The iron content in *ehb1* mutant seeds showed only slight but not statistically significant increase compared to that in the wild type; however, the seeds of the HA-EHB1 overexpressing line accumulated significantly less iron. This is consistent with the negative effect of EHB1 on iron uptake. In the case of *ehb1*, probably other mechanisms interfered with the loading of the excess iron. To test whether this effect is specific to iron, we measured the content of manganese, which is imported by a different high-affinity transporter but is also a secondary substrate of IRT1 (Korshunova et al., 1999; Vert et al., 2002). The levels o f manganese in *ehb1* mutant seeds were fully comparable to that in wild-type seeds, whereas HA-EHB1 plants showed slightly elevated manganese content. The two elements are known to be dependent on each other's transport in seeds (Chu et al., 2017), so the manganese accumulation in HA-EHB1 plants is potentially a secondary effect of compromised iron loading in these seeds. Thus, EHB1 preferentially affects the acquisition of iron at the import step, which in Arabidopsis is mediated by its interaction partner IRT1.

EHB1 Directly and Negatively Affects IRT1-Mediated Iron Import

To verify the direct connection between the negative effect of EHB1 on iron import and the function of IRT1, we reconstructed this binary system in a heterologous environment. We expressed combinations of the two proteins in yeast (*Saccharomyces cerevisiae*) cells. As a model, we employed the *fet3fet4* mutant yeast strain (Eide et al., 1996). Due to the absence of a functional multicopper oxidase FET3 and a bivalent iron transporter FET4, this strain has a severely reduced capacity of both bivalent and trivalent iron import, compared to that of wild-type yeast (Fig. 7A). Despite that, *fet3fet4*

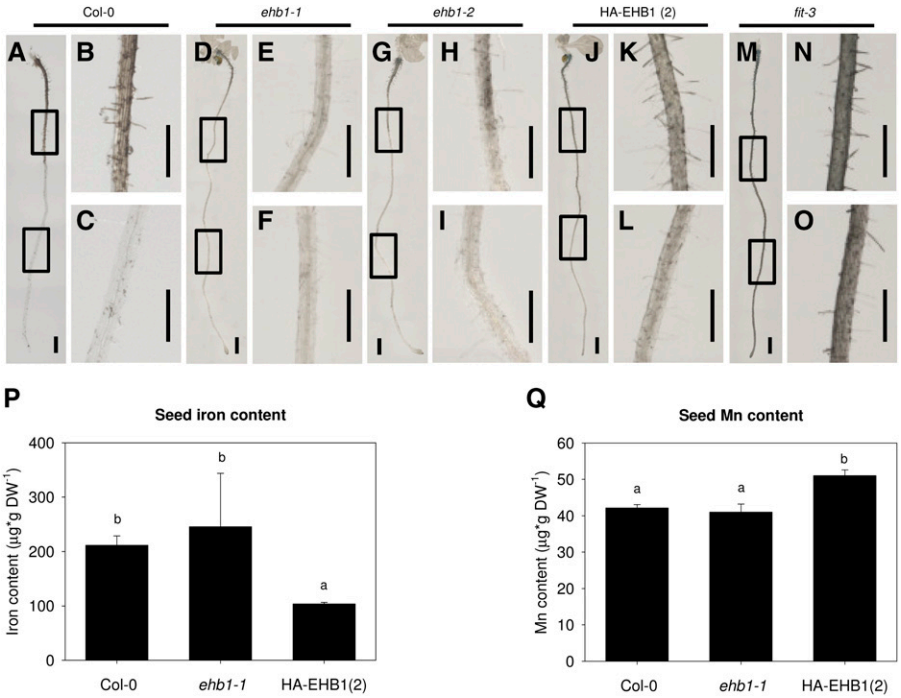

Figure 6. Iron import activity and storage in Arabidopsis depend on the presence of EHB1. A–O, Roots of wild-type (Col-0) seedlings, *ehb1* mutants, and an HA-EHB1-expressing line grown for 8 d under sufficient iron were stained for the presence of iron. The *fit-3* roots were used as a control, which cannot take up the iron available in the apoplast. Apoplastic iron is visible as dark precipitates. Rectangles in the overview images (A, D, G, J, and M) indicate the enlarged regions (B, C, E, F, H, I, K, L, N, and O). The experiment was performed three times yielding comparable results. Scale bars = 0.5 cm. P and Q, Measurement of the total iron (P) and manganese (Q) content in seeds of Col-0, *ehb1-1* and one HA-EHB1-expressing line grown on soil under standard growth conditions. DW, dry weight. Error bars = SD. Different letters above the bars indicate statistically significant difference ($P < 0.05$), $n = 3$.

retains its ferric reductase activity and, due to the presence of low-affinity iron-chelate transporters, is capable of surviving under iron-replete conditions. We performed a complementation test using the full-length IRT1 in combination with HA-tagged EHB1 forms. The expression of none of the proteins in the wild type affected yeast growth on iron-depleted medium (Fig. 7B). Unlike the wild-type control, the *fet3fet4* strain was not able to grow in the absence of iron (chelated by bathophenanthrolinedisulfonic acid [BPDS]). However, the expression of IRT1 alone was sufficient to rescue this phenotype, as previously reported (Eide et al., 1996). The addition of EHB1-HA to the system reverted almost entirely this IRT1-mediated complementation, suggesting that EHB1 is sufficient to suppress IRT1 activity. To test this, we coexpressed IRT1 with the interaction-deficient form of EHB1 lacking the CAR-signature domain. This combination led to the complementation of the iron-deficient phenotype, suggesting full activity of IRT1 in the absence of IRT1-EHB1 interaction (Fig. 7B). Because the negative effect of EHB1-HA could not be observed in the wild-type strain, we can exclude the possibility that it may affect other components of the iron acquisition system, such as the ferric reductase, for example. Therefore we can conclude that through its interaction with IRT1, which is mediated by its CAR-signature domain, EHB1 acts as a direct inhibitor of IRT1 function, leading to suppression of iron acquisition in Arabidopsis.

DISCUSSION

Although IRT1 is not the only transporter at the root surface capable of importing iron (Cailliatte et al., 2010), its controlled expression and subcellular localization in the root hair cells of the early differentiation zone (Blum et al., 2014; Marquès-Bueno et al., 2016; Dubeaux et al., 2018) make it the principal Strategy I iron importer and therefore a critical gateway for bioavailable iron. The capacity of iron to change oxidation states makes it a valuable component of many biological processes. However, its presence poses a challenge for the cell to prevent the deleterious effects of oxidative damage. In addition, IRT1 imports metals other than iron and the possibility to inhibit its function is an important step in preventing metal toxicity. Under iron deficiency, IRT1 substrates, such as zinc and manganese, might be imported and overaccumulate in the plant over time. Terminating this accumulation process might be the

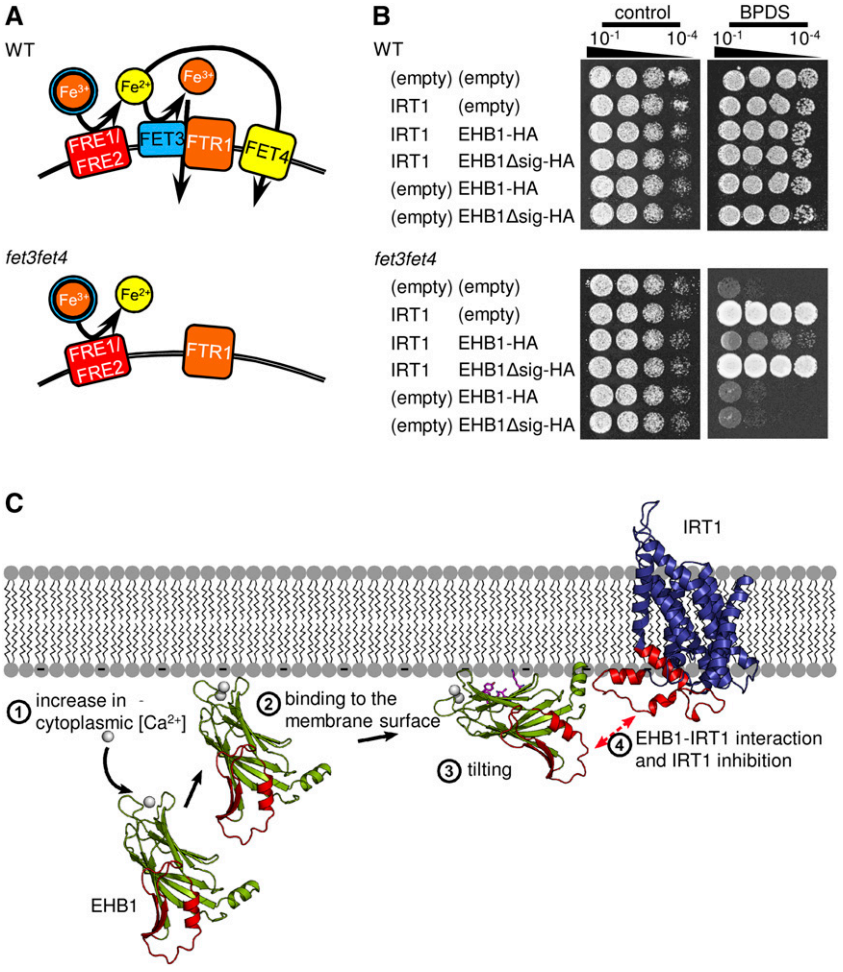

Figure 7. EHB1 inhibits IRT1-mediated iron transport. A, Schematic representation of the iron acquisition system in wild-type (WT) yeast and the modified system in the *fet3fet4* strain. FRE1 and 2, Ferric Reductase 1 and 2; FET3 and 4, Ferrous Transport 3 and 4; FTR1, Fe Transporter 1. B, Growth of wild-type and *fet3fet4* yeast on media with sufficient iron (control) and with iron-depleted (BPDS) media. The *fet3fet4* strain is not capable of growing when iron is limiting and the introduction of the Arabidopsis IRT1 can rescue this phenotype. In the presence of EHB1, IRT1 loses the capacity to rescue *fet3fet4*, whereas the EHB1Δsig form, incapable of interacting with IRT1, has no effect on IRT1-mediated iron acquisition. C, Hypothetical mechanism of the EHB1–IRT1 interaction using information from other C2 domain proteins, homology models for EHB1 and IRT1, and results from our MD simulations. Structures highlighted in red relate to protein regions identified here as relevant for the EHB1/IRT1 interaction. (1) An increase in the cytosolic calcium concentration leads to the occupation of the EHB1 calcium binding sites. This increases EHB1's affinity for the plasma membrane surface (2), which contains negatively charged phospholipids. After binding in a "perpendicular" configuration, EHB1 would tilt to favor a "parallel" interaction (3). This would bring the CAR signature domain in close proximity to the IRT1vr (4), allowing the two to interact, that way inhibiting iron uptake by a yet unknown mechanism.

major reason for having an inhibitory protein, such as EHB1, act in these conditions.

We have identified the small peripheral membrane protein EHB1 as an interactor and negative regulator of IRT1. EHB1 belongs to the 10-member CAR protein family, several members of which have a well-documented involvement in the regulation of plant responses to environmental stimuli (Knauer et al., 2011; Cheung et al., 2013; Rodriguez et al., 2014).

We showed that EHB1 exists as both a soluble and membrane-associated protein. EHB1 was found in the nucleus, the cytoplasm, and at the plasma membrane. Such localization is consistent with its influence on the IRT1 transporter, and resembles the reported subcellular localization of other CAR-family proteins (Rodriguez et al., 2014). Of special interest was the discovery that EHB1 shows a specific affinity toward phosphoinositides, such as PtdIns4P, in both an immobilized and membrane-integrated form. PtdIns4P is a very low abundant lipid enriched at the plasma membrane where it generates negative electrostatic charge critical for the attachment of regulatory proteins, such as PINOID and BRI1 KINASE INHIBITOR1 (Simon et al., 2016). We show that calcium is a critical factor in EHB1 membrane association. In the absence of calcium, the protein was unable to associate with plant microsomes. This phenomenon cannot be explained by the EHB1 phosphoinositide binding alone. The calcium-dependence of PtdIns4P and mainly PtdIns binding by EHB1 observed in the liposome-binding experiments was quantitative, rather than a complete on-off situation as seen in the fractionation experiment. This suggests that EHB1 targets additional membrane lipids. Although the exact role of calcium in EHB1 membrane binding is not yet clear, the presence of canonical calcium-coordination sites in the EHB1 C2 domain suggests its involvement in the process. In contrast to CAR1 and CAR4 proteins (Rodriguez et al., 2014), EHB1 could neither bind PC, as observed in lipid strip experiments and liposome binding studies, nor phosphatidyl-Ser (lipid strip experiment). At this point, the data suggest a diversification of target lipids within the family and argues in favor of a functional specification of CAR family members.

Our experiments in yeast showed that EHB1 affected the capacity of IRT1 to complement the iron-deficient *fet3fet4* strain. The control experiment in the wild-type strain, where EHB1 did not affect the endogenous yeast iron acquisition components, demonstrates that the EHB1 effect was due to its direct and specific inhibition of IRT1. This conclusion is also supported by the fact that Basic Local Alignment Search Tool searches revealed no EHB1 homologs, as well as no CAR-family proteins in *Saccharomyces cerevisiae*. The experiment, together with the EHB1-IRT1 interaction, shows that the observed iron acquisition phenotypes in plants with modified EHB1 presence are due to the changes in the efficiency of IRT1 caused by the presence or absence of EHB1. We cannot exclude that EHB1 affects also other components of the Arabidopsis iron acquisition system. We have observed consistent effects on the activity of the root surface ferric reductase. It may be possible that FRO2 and IRT1 form a protein complex for increased iron import efficiency, similarly to the Fet3pFtr1p complex in yeast. If so, the two proteins might influence each other's activity.

At present, the mechanism of EHB1-mediated IRT1 activity inhibition at the molecular level remains unclear. Because an experimental structure of the IRT1-EHB1 complex remains to be determined, we employed a comparative modeling combined with all-atom MD simulations to suggest an EHB1 membrane binding mode and propose an interaction mechanism between EHB1 and IRT1 (Fig. 7C). It has been previously proposed that the number of calcium ions bound to CAR proteins varies with respect to the surrounding calcium concentration (Diaz et al., 2016). An increase in calcium concentration would therefore favor interactions with negatively charged lipids in the plasma membrane, also causing increased protein concentration close to the membrane surface (Honigmann et al., 2013; Diaz et al., 2016). Increased concentrations of cytoplasmic calcium have been shown in iron-deficient roots (Tian et al., 2016); however, calcium signatures may vary in intensity and duration (Steinhorst and Kudla, 2014). In a recent study, we were able to show that a calcium-decoding unit of CALCINEURIN B-LIKE PROTEIN1/9-CIPK11 is needed to perceive elevated calcium concentrations at the plasma membrane and translate it into a specific phosphorylation mark on the transcription factor FIT, which is thus activated and upregulates iron deficiency responses (Gratz et al., 2019). Another CIPK-family member, CIPK23, was shown to specifically interact with and regulate IRT1 (Dubeaux et al., 2018). Therefore, the EHB1 membrane association and EHB1-IRT1 interaction might occur in response to specific pulses of calcium waves that trigger the events and disappear shortly after. Thus, EHB1 might represent a rapid and dynamic response mechanism for switching off iron uptake under specific conditions. This may be particularly important under sufficient iron conditions, where the expression of IRT1 is transiently triggered (Hong et al., 2013) and the possibility should exist to quickly block iron import once sufficient iron amounts have been acquired. Such EHB1 function is well supported by the enhanced *EHB1* gene expression under iron-sufficient conditions, the reduced acquisition of apoplastic iron in roots of *ehb1* mutants, and the reduced iron content in seeds of HA-EHB1–expressing plants. Calcium is a second messenger for a wide variety of environmental cues (Steinhorst and Kudla, 2014). As iron acquisition is affected by the availability of other metals in the soil (Lešková et al., 2017), it is possible that EHB1-mediated IRT1 inhibition is not limited to iron-related signaling. It might occur under other stimuli as well, and thus, it might contribute to the global plant stress response modulation in a constantly changing environment.

Our EHB1 structural model was complexed with two calcium ions, reflecting a medium-to-high surrounding

calcium concentration (Diaz et al., 2016). EHB1 bound to a membrane with a typical composition of a plant plasma membrane in all replicas of MD simulations; initially, the binding occurred with an orientation "perpendicular" (Honigmann et al., 2013) to the membrane. Under our simulation conditions, the EHB1 concentration in the water phase is rather high (~1.5 mM), which may explain why we observe binding to a membrane that lacks phosphoinositides. At the same time, the membrane does contain negatively charged DOPG, and the binding is in line with the above suggestion that EHB1 targets additional membrane lipids. The MD simulations revealed in all but one replica a potassium ion bound in proximity to the calcium binding sites, which could represent how an additional calcium ion would bind under physiological conditions. In the course of all replicas, EHB1 tended to tilt and interact with the membrane through its positively charged surface, thereby leading to a binding "parallel" to the membrane. In one replica, the tilting persisted throughout the simulation time, mainly through interactions between residues 51–62, 140–142, and 164–168 with the membrane, whereas in the other replica, EHB1 frequently exchanged between "perpendicular" and "parallel" configurations. On the one hand, the lack of phosphoinositides in our model membrane may result in the less stable "parallel" binding mode. On the other hand, the "parallel" configuration may require further interactions to become stable. We note in this context that only in the "parallel" configuration the CAR signature domain, identified here to be responsible for the interaction with IRT1, can be expected to come close to the IRT1vr, as inferred from a structural model containing both EHB1 and IRT1 at or in the membrane. For the homologous proteins PKC-α (Guerrero-Valero et al., 2009) and synaptotagmin-1 (Honigmann et al., 2013), it was shown that the "parallel" configuration is mediated by interactions between PtdIns4,5P_2 in the membrane and a polybasic patch on the protein. The close plant homologs CAR1 and CAR4 have significant differences in the site of the patch that may be responsible for a lack of specific binding to PtdIns4,5P_2 (Diaz et al., 2016). Similarly, the lack of binding of EHB1 to PtdIns4,5P_2 can, at least in part, be explained by the lack of stabilizing interactions in the polybasic region, while supporting the binding with PtdIns4P.

A plausible reason for the EHB1-mediated IRT1 inhibition may be the interaction with the IRT1 variable region. This cytoplasmically exposed stretch contains one of a total of three metal coordination sites in IRT1 (Eng et al., 1998; Rogers et al., 2000). The site may become hidden and therefore nonfunctional due to the proximity of EHB1. Additionally, two of the IRT1 transmembrane domains, IV and V, contain metal coordination sites. EHB1 interaction might force a change in their orientation, thus rendering them incapable of transferring the iron across the membrane. A second possibility for the inhibitory effect of EHB1 is based on the finding that CAR4 protein was shown to cause liposome membrane tubulation in the presence of calcium in vitro (Diaz et al., 2016). It was thus proposed that its physiological role would be to react to a calcium signature and initiate membrane curvatures serving as signaling platforms for downstream processes (Diaz et al., 2016). In the case of EHB1, a calcium-dependent tubulation of IRT1-containing membrane might promote the endocytosis of the iron transporter. This would reduce the IRT1 protein available for iron transport and therefore the iron transport efficiency. The physiological data that we present in this article are generally in agreement with such a mechanism. This includes the observation of an increased IRT1 protein abundance in the lines lacking EHB1. The two *ehb1* lines show enhanced iron import, suggesting higher abundance and enhanced stability of active IRT1. These two possible mechanisms of EHB1 function are not mutually exclusive and might happen sequentially: first EHB1-mediated IRT1 inactivation, followed by endocytosis.

In summary, our data show that the peripheral membrane protein EHB1 can interact with the iron transporter IRT1. IRT1 is the primary importer of soil iron. To prevent iron overaccumulation in the cell, the otherwise soluble EHB1 protein is recruited to the plasma membrane in a calcium-dependent manner. In addition, calcium promotes the EHB1-IRT1 interaction, which results in the inhibition of transporter activity. This represents a novel mechanism for dynamic rebalancing of metal acquisition required for the prevention of metal toxicity.

MATERIALS AND METHODS

Yeast Transformation, Media, and Selection

The coding sequence of the IRT1 variable region (IRT1vr) was amplified by PCR from cDNA obtained from iron-deficient wild-type (Col-0) roots using the primers I1LB1 and I1LB2 (Supplemental Table S1), subcloned into pDONR207 (Life Technologies) and transferred into the final destination vector pGBKT7-GW. This construct was then introduced into yeast (*Saccharomyces cerevisiae*) strain Y187 by the lithium acetate method (BD Biosciences). The resulting strain was mated with AH109 strain (BD Biosciences) harboring a cDNA library made from iron-deficient Arabidopsis (*Arabidopsis thaliana*) roots in the pGADT7 vector (Lingam et al., 2011) and plated on a double-selective Synthetic Defined (SD) medium lacking Trp (selects for presence of pGBKT7-GW:IRT1vr) and Leu (selects for presence of a library cDNA clone in pGADT7). Positive colonies were resuspended in distilled water and spread onto selection plates containing SD medium lacking Trp, Leu, and His, and supplemented with 4 mM of 3-amino-1,2,4-triazole (selection for protein–protein interaction). The plates were incubated for 10 d at 30°C and, starting from d 5, 43 newly-appeared colonies were picked, and insertions were amplified by PCR from the library-containing pGADT7 vector using primers Yeast seqF and Yeast seqR (Supplemental Table S1). For targeted yeast two-hybrid screens, EHB1 coding sequence was amplified using primers EHB1nterB1 and EHB1B2, subcloned into pDONR207, which was then used to create AD-EHB1 fusion in pACT2-GW. Yeast strain AH109 was cotransformed with AD- and BD fusion-expressing vector combinations. Cultures from the resulting transformation events were spotted in 10-fold dilutions onto SD medium-containing agar plates either lacking Trp and Leu or lacking Trp, Leu, and His, and supplemented with and 2.5 mM of 3-amino-1,2,4-triazole. Cotransformation of SNX1 AD and BD fusions, assaying for SNX1 homodimerization (Pourcher et al., 2010), was used as a positive control. Cotransformations with the respective non-recombined pACT2-GW and pGBKT7-GW were used as negative controls.

For complementation studies, the full-length *IRT1* coding sequence was amplified from cDNA obtained from iron-deficient wild-type (Col-0) roots

using primers I1B1 and FLI1B2Stop (Supplemental Table S1). The fragment was subcloned into pDONR207 and transferred to pAG426GPD-ccdB-eYFP vector (Susan Lindquist, Addgene plasmid # 14228). *EHB1* coding sequence was amplified from wild-type (Col-0) root cDNA using primers EHB1B1 and EHB1cterB2 (Supplemental Table S1) before subcloning into pDONR207 and transferred to pAG425GPD-ccdB-HA (Susan Lindquist, Addgene plasmid # 14250). Yeast strains INVSc1 (*MATa his3D1 leu2 trp1-289 ura3-52 MAT his3D1 leu2 trp1-289 ura3-52*, Thermo Fisher Scientific) and DEY1453 (*MATa/MATa ade2/+ can1/can1 his3/his3 leu2/leu2 trp1/trp1 ura3/ura3 fet3-2::HIS3/fet3-2::HIS3 fet4-1::LEU2/fet4-1::LEU2*; Eide et al., 1996) were used as hosts. To study the IRT1-mediated complementation of the DEY1453 iron-deficiency phenotype, 10-fold dilution of yeast cultures harboring combinations of IRT1 and EHB1, together with control transformants, were plated on agar plates containing yeast extract peptone dextrose medium either supplemented with 80 μM of BPDS (iron-deficient conditions) or not (control conditions). Yeast growth was observed on d 3 after plating. Identical experiment in the INVSc1 strain was used to exclude any potential adverse effects to yeast growth from the expression of the constructs in the absence of the iron uptake-related mutations.

BiFC and Protein Localization

The 2in1 BiFC vector system was used to visualize protein–protein interactions in transiently transformed (*Nicotiana benthamiana*) epidermis cells. Full-length *EHB1* sequence was amplified from cDNA using primers EHB1B3 and EHB1cterB2. *EHB1Δsig* was created in a two-step reaction, first the *EHB1* coding sequence fragments neighboring the CAR signature domain were amplified in separate reactions using primers EHB1B3 and E1ΔSig1, and E1ΔSig2 and EHB1cterB2. In a second step, *EHB1Δsig* was amplified using primers EHB1B3 and EHB1cterB2, and the two fragments from the first step as a template. The *EHB1* and *EHB1Δsig* fragments were subcloned in pDONR221-B3B2 vector (Life Technologies). Primers for the amplification of the IRT1vr deletions were as follows: *IRT1vr*, I1LatgB1 and I1LnsB4; *IRT1vrΔ1*, I1LatgB1 and 2cternsB4; *IRT1vrΔ2*, 3cterB1 and I1LnsB4; *IRT1vrΔ3*, 4cterB1 and 4cternsB4. The *IRT1vrΔHis* fragment was created in a two-step reaction as described for *EHB1Δsig*. The first-step amplifications were made using the primer pairs I1LatgB1 and 5AM1, and 5BM2 and I1LnsB4. The second reaction was performed with primers I1LatgB1 and I1LnsB4. All *IRT1vr* fragments were subcloned into pDONR221-P1P4 vector (Life Technologies). Combinations of *EHB1* and *IRT1vr* fragments were inserted into vector pBiFCt-2in1-CC vector (Grefen and Blatt, 2012) by recombination.

For investigating EHB1 localization, the full-length *EHB1* sequence was amplified from cDNA using primers EHB1B1 and EHB1cterB2, subcloned into pDONR207 (Life Technologies) and introduced by recombination to pMDC83 (Curtis and Grossniklaus, 2003). *GFP6* sequence was amplified from pMDC83 using primers G6B1 and G6B2, subcloned into pDONR207 (Life Technologies) and introduced by recombination to pMDC7 (Curtis and Grossniklaus, 2003). IRT1-mCherry fusion was expressed from the pJNC1:IRT1 vector (Ivanov et al., 2014), and AHA1-mRFP was expressed from the pB7WG2:AHA1 vector (Caesar et al., 2011).

Final vectors were introduced into *N. benthamiana* through a *Rhizobium radiobacter*-mediated transformation (Hötzer et al., 2012) and fluorescence was investigated under a microscope. GFP expression was induced 24 h after infiltration by treating the leaf with 20 μM of β-estradiol (Sigma-Aldrich) in dimethyl sulfoxide with 0.1% (w/v) TWEEN 20 (Sigma-Aldrich).

All mentioned primers are listed in Supplemental Table S1.

Fluorescence and Confocal Microscopy

For standard fluorescence imaging, AxioImager 2 microscope (Zeiss) equipped with the ApoTome.2 module was used. Images were taken with a Plan-Apochromat 40×/1.4 Oil objective and recorded by an Axiocam 503 monochromatic camera (Zeiss). Filter sets were as follows: GFP: Filter set 38 HE eGFP shift free (E) [EX BP 470/40, BS FT 495, EM BP 525/50]; YFP: Filter set 46 HE YFP shift free (E) [EX BP 500/25, BS FT 515, EM BP 535/30]; mCherry: Filter set 43 HE Cy 3 shift free (E) [EX BP 550/25, BS FT 570, EM BP 605/70].

Confocal microscopy was performed on an LSM 780 (Zeiss). For GFP visualization, excitation at 488 nm and detection between 505 and 545 nm were used. For mRFP/mCherry, excitation at 561 nm and detection from 575 to 615 nm were used. Pinholes for both channels were set to 1 Airy Unit resulting in optical slices of 0.8 mm. Images were recorded in a 1,024-pixel format. Colocalization analysis was performed on 8-bit grayscale image pairs, representing the GFP and mRFP/mCherry channels. Images were loaded in the software ImageJ (http://rsb.info.nih.gov/ij) and analyzed using the JACoP v2.0 plug-in (Bolte and Cordelières, 2006). Threshold values were automatically adjusted by the software.

Protein Expression and Purification

EHB1 coding sequence was amplified from cDNA using primers E1*Spe*IFw and E1*Xho*IRev containing *Spe*I and *Xho*I restriction sites, respectively (Supplemental Table S1). The fragment was digested by the two nucleases, purified and inserted into the *Spe*I and *Xho*I sites of the pET-StrepII vector (Novagen). The resulting pET-StrepII:EHB1 vector was introduced into BL21(DE3) cells (New England BioLabs). For StrepII-EHB1 fusion protein expression, a culture with OD_{600} 0.6 was induced by 0.1 mM of isopropyl β-D-1-thiogalactopyranoside. Cells were collected 3 h after the induction and lysed in a buffer containing 100 mM of Tris-HCl at pH 8.0, 150 mM of NaCl, 5 mM of 1,4-dithiothreitol, 0.35 mg/mL of lysozyme, 1 mM of Brij-35, and 1× CIP protease inhibitor (Roche). After 30 min, 0.1% (w/v) of Triton X-100 was added and the suspension was sonicated. StrepII-EHB1 was solubilized in the presence of 100 mM of Tris-HCl at pH 8.0, 150 mM of NaCl, 1 mM of Brij-35, and 8 M of Urea. The unspecific biotin-binding sites were blocked by the addition of avidin to a concentration of 100 μg/mL. The solution was then diluted 10-fold in 100 mM of Tris-HCl at pH 8.0 and 1 mM of Brij-35 before the addition of Strep-Tactin Macro Prep suspension (IBA Life Sciences). The beads were washed in 100 mM of Tris-HCl at pH 8.0, 150 mM of NaCl, and 1 mM of Brij-35 and then eluted in the same buffer in the presence of 2.5 mM of α-Desthiobiotin.

Protein Coimmunoprecipitation

N. benthamiana epidermis was transformed as above with combinations of IRT1-GFP and EHB1-HA or EHB1Δsig-HA expressing vectors. To create the *EHB1-HA* expression cassette, the EHB1 coding sequence was amplified from cDNA using the EHB1B1 and EHB1cterB2 primers (Supplemental Table S1) introduced to pDONR207 and then transferred to pAUL1 vector (Lyska et al., 2013). The same cloning strategy was used for the generation of the *EHB1Δsig-HA* cassette. One gram of plant material was ground under liquid nitrogen and resuspended in immunoprecipitation (IP) buffer (50 mM of Tris HCl at pH 8.0, 150 mM of NaCl, 1 mM of EDTA, 1% [w/v] Triton-x-100, and 1× CIP protease inhibitor; Roche). Where indicated, 100 mM of $CaCl_2$ was added to the IP buffer. The cell debris was removed by centrifugation for 10 min (16,800*g*, 4°C). GFP-Trap_A beads (ChromoTek) were washed twice in IP buffer and resuspended to a final volume of 100 μL. The supernatant was incubated with 25 μL of the beads suspension at a revolving wheel for 3 h at 4°C. Beads were collected by centrifugation and washed three times with 1-mL IP buffer each. Elution was done using 50-μL SDG buffer (62 mM of Tris-HCl at pH 8.6, 2.5% [w/v] SDS, 2% [w/v] 1,4-dithiothreitol, and 10% [v/v] glycerol) at room temperature. Samples were taken from the original cleared extract (designated "input") and after elution (designated "IP"). The experiments were repeated twice, yielding comparable results.

SDS-PAGE and Immunoblot

Protein electrophoresis and protein immunoblots were performed as described in Ivanov et al. (2014). For electrophoresis, 4% to 20% 10-well Mini-Protean stain-free gradient gels (Bio-Rad) were used. The antibody dilutions were as follows: mouse anti-GFP (11814460001; Roche) 1:1,000, mouse anti-actin (MabGPa; Sigma-Aldrich) 1:1,000, rabbit anti-IRT1 (AS11 1780; Agrisera) 1:5,000, rabbit anti-PM(H^+)-ATPase (AS07 260; Agrisera) 1:1,000, rabbit anti-UGPase (AS05 086; Agrisera) 1:1,000, rat monoclonal anti-HA horseradish peroxidase conjugated (3F10; Roche) 1:5,000, goat anti-mouse IgG horseradish peroxidase (W4011; Promega) 1:5,000, and goat anti-rabbit IgG horseradish peroxidase (AS09 602; Agrisera) 1:5,000. StrepII-tag was detected using Strep-Tactin horseradish peroxidase conjugate (IBA Life Sciences) at a dilution of 1:1,000.

Lipid Overlay and Liposome Binding Assays

The Membrane Lipid Strip (Echelon) membrane was blocked for 3 h with 3% (w/v) fatty acid-free bovine serum albumin (Sigma-Aldrich) in Tris-buffered saline with TWEEN 20 (20 mM of Tris-HCl at pH 7.4, 180 mM of NaCl, 0.1% [w/v] Tween 20) buffer and then incubated overnight with the purified StrepII-EHB1

protein (2 μg/mL). The presence of immobilized StrepII-EHB1 was detected using Strep-Tactin horseradish peroxidase conjugate (IBA Life Sciences). Where indicated, the Tris-buffered saline with TWEEN 20 buffer contained an additional 100 μM of $CaCl_2$.

For the liposome-binding assay, PC or a 75:25 (w/w) mixture of PC:PtdIns, or PC:PtdIns4P (Sigma-Aldrich) was prepared. A 2% (w/v) lipid suspension was prepared in a buffer containing 50-mM HEPES and 100 mM of NaCl at pH 6.8 by sonication and frozen. Upon defreezing, the suspension was additionally sonicated and the resulting liposomes were extruded through a 0.2-μm pore size polycarbonate membrane using a Mini Extruder (Avanti Polar Lipids). The liposomes were incubated with 5 μg of purified StrepII-EHB1 for 30 min at 30°C in the above HEPES-NaCl buffer. The suspension was then centrifuged at 100,000*g* for 30 min in a SW40Ti Swinging Rotor (Beckman). Supernatant and resuspended pellet were collected and analyzed for the presence of StrepII-EHB1. Where indicated, the buffer contained an additional 100 μM of $CaCl_2$. The experiments were performed three times with new lipid membranes or freshly prepared liposomes, yielding comparable results.

Isolation of Membrane Fractions

Roots of HA-EHB1-expressing Arabidopsis plants, grown in the 2-week growth system, were used in the experiment. The separation of microsomal and soluble fractions was performed as described in Alexandersson et al. (2008), except that where indicated the buffer contained additional 100-μM $CaCl_2$. Equal amounts of soluble and microsomal fraction were loaded for analysis. The experiment was performed three independent times and yielded comparable results.

Immunoblot Band Intensity Quantification

Densitometry analysis of immunoblot images was performed using the software ImageJ (National Institutes of Health) as described in Ivanov et al. (2012b).

Homology Modeling and MD Simulations

EHB1 and IRT1 (UniProt accession IDs Q9S764 and Q38856, respectively) were modeled with the software TopModel (Mulnaes and Gohlke, 2018) as described in Milić et al. (2018). EHB1 was modeled based on structures with PDB IDs 4V29 and 5A52 (46.9% and 52.2% of sequence identity, respectively; in both cases, chain "A" was used). For IRT1, only PDB ID 5TSA was identified as a template (15.5% sequence identity; chain "A" was used), and the first 50 residues were omitted as no coverage for this portion was available.

MD simulations were prepared to evaluate the binding mode of EHB1 with respect to a membrane. The system was prepared with the tool Packmol-Memgen (Case et al., 2018), placing the protein at ~25 Å from the membrane surface. The membrane composition was 4:4:1 DOPC/DOPE/DOPG, resembling main components of a plant plasma membrane (Furt et al., 2011). Two calcium sites of EHB1 were occupied by using the coordinates found in the crystal structure of PDB ID 4V29. The system charges were neutralized by adding 0.15 M of KCl in the solvation box. The GPU implementation of the program AMBER18 pmemd (Darden et al., 1993; Le Grand et al., 2013) with the ff14SB (Maier et al., 2015) and the software Lipid17 (Dickson et al., 2014; Skjevik et al., 2014; Case et al., 2018) parameters for the protein and the membrane lipids, respectively, were used. Water molecules were added using the TIP3P model (Jorgensen et al., 1983). After thermalization to 300 K and density adaptation, five independent MD simulations of 1-μs length were performed in the NPT ensemble. Covalent bonds to hydrogens were constrained with the SHAKE algorithm (Ryckaert et al., 1977) in all simulations, allowing use of a time step of 2 fs.

To obtain a representative depiction of IRT1 embedded in the membrane, the homology model of IRT1 was treated with the same MD protocol as EHB1, simulating five replicas for 500 ns. The structure considered is a representative conformation of the biggest cluster identified by using the Density-based spatial clustering of applications with noise (DBSCAN) algorithm with an ε-parameter of 1 Å across the last 200 ns of all replicas. All analyses were performed with the software CPPTRAJ (Roe and Cheatham, 2013).

Plant Material

The Arabidopsis *ehb1-1*, *ehb1-2* (Knauer et al., 2011), and *irt1-1* (Vert et al., 2002) mutants were previously described. Absence of a full-length transcript in *ehb1-1* and *ehb1-2* was verified by PCR on cDNA from the two mutants, as well as on wild-type and HA-EHB1 cDNA. PCR was performed using primers EHB1f and EHB1r (Supplemental Table S1). For the generation of the HA-EHB1 lines, full-length EHB1 fragment was amplified from cDNA using primers EHB1nterB1 and EHB1B2 (Supplemental Table S1), subcloned into pDONR207 vector (Life Technologies) and transferred to pAlligator-2 vector by recombination. The resulting vector was introduced into *R. radiobacter* C58C1 (pGV2260) strain. Transformation of Arabidopsis wild-type Col-0 ecotype was performed using the floral dip method (Clough and Bent, 1998). Homozygous T4 plants were used in the study.

Plant Growth Conditions

Arabidopsis plants were surface-sterilized and grown upright on agar plates containing Hoagland medium as in Brumbarova and Ivanov (2016). The medium either contained 50-μM FeNaEDTA (50-μM Fe, sufficient iron condition) or FeNaEDTA was omitted (0-μM Fe, iron-deficient conditions). Plants were either grown directly on 50-μM Fe or 0-μM Fe plates for 8 d (referred to as "8-d growth system"), or were grown on 50-μM Fe plates for 14 d and then separated to either 50-μM Fe or 0-μM Fe plates for three additional days (referred to as "2-week growth system").

For localization and interaction analysis in leaf epidermis, *N. benthamiana* plants were germinated on soil and grown for 3 weeks in a greenhouse. When needed, artificial light was used to ensure a 16-h day and 8-h night cycle.

Histochemical Detection of Iron

The visualization of iron in roots of plants, grown in the 8-d growth system, was performed using the Perls-3,3′-diaminobenzidine tetrahydrochloride method, as described in Brumbarova and Ivanov (2014). The stained roots were imaged on AxioImager.M2 microscope (Zeiss) at 20× magnification using the "Tiles" module and the "stitching" function of the software ZEN 2 (Zeiss) to assemble the collected images. The experiment was performed on three independently grown batches of plants, yielding comparable results.

Chlorophyll Content Measurement

Leaves were collected from plants grown in the 2-week growth system. Chlorophyll content was analyzed as described in Ivanov et al. (2014). The experiment was performed on five independently grown sets of plants.

Measurement of Ferric Reductase Activity

Plants were grown in the 2-week growth system. The activity of the root surface ferric reductase was measured spectrophotometrically as described in Le et al. (2016). The experiment was performed on five independently grown sets of plants.

Measurement of Root Length

Root length was measured from frontal images of plant roots using the JMicroVision software (http://www.jmicrovision.com) as described in Ivanov et al. (2014). A minimum of 25 plants were measured per genotype per condition. The whole experiment was performed on five independently grown sets of plants.

Gene Expression Analysis by Reverse-Transcription Quantitative PCR

Total RNA was prepared from Arabidopsis plants grown in the 2-week growth system using the RNeasy Plant Mini Kit (Qiagen). Oligo dT primer and RevertAid first-strand cDNA synthesis kit (Thermo Fisher Scientific) were used for cDNA preparation. Reactions were prepared with DyNAmo ColorFlash SYBR Green qPCR Kit (Thermo Fisher Scientific) and were carried out in a C100 Touch PCR Cycler equipped with the CFX96 Real-Time System (Bio-Rad). Data were analyzed with the software CFX Manager (Bio-Rad). Reactions using mass standard dilution series for each gene were used to generate standard curves, based on which the quantification of the samples was done. Samples were normalized to the expression of *EF1Bα*. Amplification of the unspliced form of *EF1Bα* was used to control for genomic DNA contamination. The

experiment was performed on three independently grown sets of plants with each cDNA sample analyzed in two replicates to control for technical variations. Primer sequences for all analyzed genes are available in Supplemental Table S1.

Fe and Mn Content Measurement

Seed samples of soil-grown plants were ground and melted at high temperature in a solution of 65% (v/v) HNO_3:30% (v/v) H_2O_2 = 5:2. The cooled solutions were measured with inductively coupled plasma optical emission spectrometry (conical atomizer; 0.61 l/min argon flow; pressure: 2.41 bar, Ultima 2; HORIBA Jobin Yvon). The wavelengths used were as follows: Fe = 259.940 nm; Mn = 257.610 nm. Three independent batches of seeds were measured.

Statistical Analysis

For statistical analysis, data were analyzed using one-way ANOVA followed by Fisher's least significant difference post hoc test in the software SPSS Statistics (IBM). The obtained *P* values were used for identifying statistically significant differences between groups ($P < 0.05$).

Accession Numbers

CAR1, At5g37740; *CAR4*, At3g17980; *EF1Bα*, At5g19510; *EHB1*, At1g70800; *FER*, At5g01600; *FIT*, At2g28160; *FRO2*, At1g01580; *IRT1*, At4g19690; *SNX1*, At5g06140; PKC-α, GC17P066302.

Data Availability

Data supporting the findings of this study are available within the article and its Supplemental Data, and from the corresponding author on request.

Supplemental Data

The following supplemental information is available.

Supplemental Figure S1. Heterologous expression and purification of StrepII-EHB1 and StrepII-EHB1Δsig in *E. coli*.

Supplemental Figure S2. Binding of StrepII-EHB1Δsig to membrane lipids.

Supplemental Figure S3. Generation of HA-EHB1–expressing Arabidopsis plants.

Supplemental Figure S4. The *ehb1* T-DNA insertion mutants used in this study.

Supplemental Figure S5. Gene expression analysis in the *ehb1-2* mutant.

Supplemental Table S1. Primers used in this study.

Supplemental Movie. MD simulation of EHB1 membrane binding.

ACKNOWLEDGMENTS

We thank Dr. Christoph Forreiter for the *ehb1* mutants, Dr. Christopher Grefen for the pBiFCt-2in1 vectors, Prof. Klaus Harter for the pB7WG2:AHA1 vector, Dr. Yves Jacob for the pACT2-GW and pGBKT7-GW vectors, Dr. Nicole Linka for help in the liposome preparation, Dr. Francois Parcy for the pAlligator-2 vector, and Prof. Peter Westhoff for the pAUL1 vector. We thank Sarah Knitter, Karolin Montag, and Daniela Lichtblau for help in cloning. We are grateful to the Jülich Supercomputing Centre at the Forschungszentrum Jülich for computing time on the supercomputers JURECA and JUWELS (NIC project ID: HKF7) and to the Zentrum für Informations und Medientechnologie at the Heinrich Heine University Düsseldorf for computational support.

Received February 13, 2019; accepted April 12, 2019; published April 30, 2019.

LITERATURE CITED

Alexandersson E, Gustavsson N, Bernfur K, Karlsson A, Kjellbom P, Larsson C (2008) Purification and proteomic analysis of plant plasma membranes. Methods Mol Biol **432:** 161–173

Barberon M, Zelazny E, Robert S, Conéjéro G, Curie C, Friml J, Vert G (2011) Monoubiquitin-dependent endocytosis of the iron-regulated transporter 1 (IRT1) transporter controls iron uptake in plants. Proc Natl Acad Sci USA **108:** E450–E458

Barberon M, Dubeaux G, Kolb C, Isono E, Zelazny E, Vert G (2014) Polarization of IRON-REGULATED TRANSPORTER1 (IRT1) to the plant-soil interface plays crucial role in metal homeostasis. Proc Natl Acad Sci USA **111:** 8293–8298

Blum A, Brumbarova T, Bauer P, Ivanov R (2014) Hormone influence on the spatial regulation of *IRT1* expression in iron-deficient *Arabidopsis thaliana* roots. Plant Signal Behav **9:** e28787

Bolte S, Cordelières FP (2006) A guided tour into subcellular colocalization analysis in light microscopy. J Microsc **224:** 213–232

Briat JF, Dubos C, Gaymard F (2015) Iron nutrition, biomass production, and plant product quality. Trends Plant Sci **20:** 33–40

Brumbarova T, Ivanov R (2014) Perls staining for histochemical detection of iron in plant samples. Bio Protoc **4:** e1245

Brumbarova T, Ivanov R (2016) Differential gene expression and protein phosphorylation as factors regulating the state of the Arabidopsis SNX1 protein complexes in response to environmental stimuli. Front Plant Sci **7:** 1456

Brumbarova T, Bauer P, Ivanov R (2015) Molecular mechanisms governing Arabidopsis iron uptake. Trends Plant Sci **20:** 124–133

Caesar K, Elgass K, Chen Z, Huppenberger P, Witthöft J, Schleifenbaum F, Blatt MR, Oecking C, Harter K (2011) A fast brassinolide-regulated response pathway in the plasma membrane of *Arabidopsis thaliana*. Plant J **66:** 528–540

Cailliatte R, Schikora A, Briat JF, Mari S, Curie C (2010) High-affinity manganese uptake by the metal transporter NRAMP1 is essential for Arabidopsis growth in low manganese conditions. Plant Cell **22:** 904–917

Case DA, Ben-Shalom IY, Brozell SR, Cerutti DS, Cheatham III TE, Cruzeiro VWD, Darden TA, Duke RE, Ghoreishi DMK, Gilson G, et al (2018) AMBER 2018. University of California, San Francisco, CA

Cheung MY, Zeng NY, Tong SW, Li WY, Xue Y, Zhao KJ, Wang C, Zhang Q, Fu Y, Sun Z, et al (2008) Constitutive expression of a rice GTPase-activating protein induces defense responses. New Phytol **179:** 530–545

Cheung MY, Xue Y, Zhou L, Li MW, Sun SS, Lam HM (2010) An ancient P-loop GTPase in rice is regulated by a higher plant-specific regulatory protein. J Biol Chem **285:** 37359–37369

Cheung MY, Li MW, Yung YL, Wen CQ, Lam HM (2013) The unconventional P-loop NTPase OsYchF1 and its regulator OsGAP1 play opposite roles in salinity stress tolerance. Plant Cell Environ **36:** 2008–2020

Chu HH, Car S, Socha AL, Hindt MN, Punshon T, Guerinot ML (2017) The Arabidopsis MTP8 transporter determines the localization of manganese and iron in seeds. Sci Rep **7:** 11024

Clough SJ, Bent AF (1998) Floral dip: A simplified method for Agrobacterium-mediated transformation of *Arabidopsis thaliana*. Plant J **16:** 735–743

Curtis MD, Grossniklaus U (2003) A Gateway cloning vector set for high-throughput functional analysis of genes in planta. Plant Physiol **133:** 462–469

Darden TA, York D, Pedersen L (1993) Particle mesh Ewald: An N·log(N) method for Ewald sums in large systems. J Chem Phys **98:** 10089–10092

Demir F, Horntrich C, Blachutzik JO, Scherzer S, Reinders Y, Kierszniowska S, Schulze WX, Harms GS, Hedrich R, Geiger D, et al (2013) Arabidopsis nanodomain-delimited ABA signaling pathway regulates the anion channel SLAH3. Proc Natl Acad Sci USA **110:** 8296–8301

Diaz M, Sanchez-Barrena MJ, Gonzalez-Rubio JM, Rodriguez L, Fernandez D, Antoni R, Yunta C, Belda-Palazon B, Gonzalez-Guzman M, Peirats-Llobet M, et al (2016) Calcium-dependent oligomerization of CAR proteins at cell membrane modulates ABA signaling. Proc Natl Acad Sci USA **113:** E396–E405

Dickson CJ, Madej BD, Skjevik AA, Betz RM, Teigen K, Gould IR, Walker RC (2014) Lipid14: The AMBER lipid force field. J Chem Theory Comput **10:** 865–879

Dubeaux G, Neveu J, Zelazny E, Vert G (2018) Metal sensing by the IRT1 transporter-receptor orchestrates its own degradation and plant metal nutrition. Mol Cell **69:** 953–964

Dümmer M, Michalski C, Essen LO, Rath M, Galland P, Forreiter C (2016) EHB1 and AGD12, two calcium-dependent proteins affect gravitropism antagonistically in *Arabidopsis thaliana*. J Plant Physiol **206:** 114–124

Eide D, Broderius M, Fett J, Guerinot ML (1996) A novel iron-regulated metal transporter from plants identified by functional expression in yeast. Proc Natl Acad Sci USA **93:** 5624–5628

Eng BH, Guerinot ML, Eide D, Saier MH, Jr. (1998) Sequence analyses and phylogenetic characterization of the ZIP family of metal ion transport proteins. J Membr Biol **166:** 1–7

Fourcroy P, Tissot N, Gaymard F, Briat JF, Dubos C (2016) Facilitated Fe nutrition by phenolic compounds excreted by the Arabidopsis ABCG37/PDR9 transporter requires the IRT1/FRO2 high-affinity root Fe^{2+} transport system. Mol Plant **9:** 485–488

Furt F, Simon-Plas F, Mongrand S (2011) Lipids of the plant plasma membrane. *In* AS Murphy, B Schulz, W Peer, eds, The Plant Plasma Membrane. Springer, Heidelberg, pp 3–30

Giehl RF, von Wirén N (2014) Root nutrient foraging. Plant Physiol **166:** 509–517

Gratz R, Manishankar P, Ivanov R, Koster P, Mohr I, Trofimov K, Steinhorst L, Meiser J, Mai HJ, Drerup M, et al (2019) CIPK11-dependent phosphorylation modulates FIT activity to promote Arabidopsis iron acquisition in response to calcium signaling. Dev Cell **48:** 726–740

Grefen C, Blatt MR (2012) A 2in1 cloning system enables ratiometric bimolecular fluorescence complementation (rBiFC). Biotechniques **53:** 311–314

Guerinot ML, Yi Y (1994) Iron: Nutritious, noxious, and not readily available. Plant Physiol **104:** 815–820

Guerrero-Valero M, Ferrer-Orta C, Querol-Audí J, Marin-Vicente C, Fita I, Gómez-Fernández JC, Verdaguer N, Corbalán-García S (2009) Structural and mechanistic insights into the association of PKCα-C2 domain to PtdIns(4,5)P2. Proc Natl Acad Sci USA **106:** 6603–6607

Haak DC, Fukao T, Grene R, Hua Z, Ivanov R, Perrella G, Li S (2017) Multilevel regulation of abiotic stress responses in plants. Front Plant Sci **8:** 1564

Hanikenne M, Krämer U, Demoulin V, Baurain D (2005) A comparative inventory of metal transporters in the green alga *Chlamydomonas reinhardtii* and the red alga *Cyanidioschizon merolae*. Plant Physiol **137:** 428–446

Hong S, Kim SA, Guerinot ML, McClung CR (2013) Reciprocal interaction of the circadian clock with the iron homeostasis network in Arabidopsis. Plant Physiol **161:** 893–903

Honigmann A, van den Bogaart G, Iraheta E, Risselada HJ, Milovanovic D, Mueller V, Müllar S, Diederichsen U, Fasshauer D, Grubmüller H, et al (2013) Phosphatidylinositol 4,5-bisphosphate clusters act as molecular beacons for vesicle recruitment. Nat Struct Mol Biol **20:** 679–686

Hötzer B, Ivanov R, Brumbarova T, Bauer P, Jung G (2012) Visualization of Cu^{2+} uptake and release in plant cells by fluorescence lifetime imaging microscopy. FEBS J **279:** 410–419

Ivanov R, Bauer P (2017) Sequence and coexpression analysis of iron-regulated ZIP transporter genes reveals crossing points between iron acquisition strategies in green algae and land plants. Plant Soil **418:** 61–73

Ivanov R, Brumbarova T, Bauer P (2012a) Fitting into the harsh reality: Regulation of iron-deficiency responses in dicotyledonous plants. Mol Plant **5:** 27–42

Ivanov R, Tiedemann J, Czihal A, Baumlein H (2012b) Transcriptional regulator AtET2 is required for the induction of dormancy during late seed development. J Plant Physiol **169:** 501–508

Ivanov R, Brumbarova T, Blum A, Jantke AM, Fink-Straube C, Bauer P (2014) SORTING NEXIN1 is required for modulating the trafficking and stability of the Arabidopsis IRON-REGULATED TRANSPORTER1. Plant Cell **26:** 1294–1307

Jorgensen WL, Chandrasekhar J, Madura JD, Impey RD, Klein ML (1983) Comparison of simple potential functions for simulating liquid water. J Chem Phys **79:** 926–935

Knauer T, Dümmer M, Landgraf F, Forreiter C (2011) A negative effector of blue light-induced and gravitropic bending in Arabidopsis. Plant Physiol **156:** 439–447

Korshunova YO, Eide D, Clark WG, Guerinot ML, Pakrasi HB (1999) The IRT1 protein from *Arabidopsis thaliana* is a metal transporter with a broad substrate range. Plant Mol Biol **40:** 37–44

Le CT, Brumbarova T, Ivanov R, Stoof C, Weber E, Mohrbacher J, Fink-Straube C, Bauer P (2016) ZINC FINGER OF ARABIDOPSIS THALIANA12 (ZAT12) interacts with FER-LIKE IRON DEFICIENCY-INDUCED TRANSCRIPTION FACTOR (FIT) linking iron deficiency and oxidative stress responses. Plant Physiol **170:** 540–557

Le Grand S, Götz AW, Walker RC (2013) SPFP: Speed without compromise—A mixed precision model for GPU accelerated molecular dynamics simulations. Comput Phys Commun **184:** 374–380

Lešková A, Giehl RFH, Hartmann A, Fargašová A, von Wirén N (2017) Heavy metals induce iron deficiency responses at different hierarchic and regulatory levels. Plant Physiol **174:** 1648–1668

Li L, Shin OH, Rhee JS, Araç D, Rah JC, Rizo J, Südhof T, Rosenmund C (2006) Phosphatidylinositol phosphates as co-activators of Ca^{2+} binding to C2 domains of synaptotagmin 1. J Biol Chem **281:** 15845–15852

Liberman LM, Sparks EE, Moreno-Risueno MA, Petricka JJ, Benfey PN (2015) MYB36 regulates the transition from proliferation to differentiation in the Arabidopsis root. Proc Natl Acad Sci USA **112:** 12099–12104

Lingam S, Mohrbacher J, Brumbarova T, Potuschak T, Fink-Straube C, Blondet E, Genschik P, Bauer P (2011) Interaction between the bHLH transcription factor FIT and ETHYLENE INSENSITIVE3/ETHYLENE INSENSITIVE3-LIKE1 reveals molecular linkage between the regulation of iron acquisition and ethylene signaling in Arabidopsis. Plant Cell **23:** 1815–1829

Lyska D, Engelmann K, Meierhoff K, Westhoff P (2013) pAUL: A gateway-based vector system for adaptive expression and flexible tagging of proteins in Arabidopsis. PLoS One **8:** e53787

Maier JA, Martinez C, Kasavajhala K, Wickstrom L, Hauser KE, Simmerling C (2015) ff14SB: Improving the accuracy of protein side chain and backbone parameters from ff99SB. J Chem Theory Comput **11:** 3696–3713

Marquès-Bueno MDM, Morao AK, Cayrel A, Platre MP, Barberon M, Caillieux E, Colot V, Jaillais Y, Roudier F, Vert G (2016) A versatile multisite Gateway-compatible promoter and transgenic line collection for cell type-specific functional genomics in Arabidopsis. Plant J **85:** 320–333

Milić D, Dick M, Mulnaes D, Pfleger C, Kinnen A, Gohlke H, Groth G (2018) Recognition motif and mechanism of ripening inhibitory peptides in plant hormone receptor ETR1. Sci Rep **8:** 3890

Mulnaes D, Gohlke H (2018) TopScore: Using deep neural networks and large diverse data sets for accurate protein model quality assessment. J Chem Theory Comput **14:** 6117–6126

Pourcher M, Santambrogio M, Thazar N, Thierry AM, Fobis-Loisy I, Miège C, Jaillais Y, Gaude T (2010) Analyses of sorting nexins reveal distinct retromer-subcomplex functions in development and protein sorting in *Arabidopsis thaliana*. Plant Cell **22:** 3980–3991

Reyt G, Boudouf S, Boucherez J, Gaymard F, Briat JF (2015) Iron- and ferritin-dependent reactive oxygen species distribution: Impact on Arabidopsis root system architecture. Mol Plant **8:** 439–453

Robinson NJ, Procter CM, Connolly EL, Guerinot ML (1999) A ferric-chelate reductase for iron uptake from soils. Nature **397:** 694–697

Rodriguez L, Gonzalez-Guzman M, Diaz M, Rodrigues A, Izquierdo-Garcia AC, Peirats-Llobet M, Fernandez MA, Antoni R, Fernandez D, Marquez JA, et al (2014) C2-domain abscisic acid-related proteins mediate the interaction of PYR/PYL/RCAR abscisic acid receptors with the plasma membrane and regulate abscisic acid sensitivity in Arabidopsis. Plant Cell **26:** 4802–4820

Roe DR, Cheatham III TE (2013) PTRAJ and CPPTRAJ: Software for processing and analysis of molecular dynamics trajectory data. J Chem Theory Comput **9:** 3084–3095

Rogers EE, Eide DJ, Guerinot ML (2000) Altered selectivity in an Arabidopsis metal transporter. Proc Natl Acad Sci USA **97:** 12356–12360

Römheld V, Marschner H (1983) Mechanism of iron uptake by peanut plants: I. Fe reduction, chelate splitting, and release of phenolics. Plant Physiol **71:** 949–954

Ryckaert J-P, Ciccotti G, Berendsen HJC (1977) Numerical integration of the Cartesian equations of motion of a system with constraints: Molecular dynamics of n-alkanes. J Comput Phys **23:** 327–341

Shin LJ, Lo JC, Chen GH, Callis J, Fu H, Yeh KC (2013) IRT1 degradation factor1, a ring E3 ubiquitin ligase, regulates the degradation of iron-regulated transporter1 in Arabidopsis. Plant Cell **25:** 3039–3051

Simon ML, Platre MP, Marquès-Bueno MM, Armengot L, Stanislas T, Bayle V, Caillaud MC, Jaillais Y (2016) A PtdIns(4)P-driven electrostatic field controls cell membrane identity and signalling in plants. Nat Plants **2:** 16089

Skjevik AA, Mileni M, Baumann A, Halskau O, Teigen K, Stevens RC, Martinez A (2014) The N-terminal sequence of tyrosine hydroxylase is a conformationally versatile motif that binds 14-3-3 proteins and membranes. J Mol Biol **426:** 150–168

Steinhorst L, Kudla J (2014) Signaling in cells and organisms—calcium holds the line. Curr Opin Plant Biol **22:** 14–21

Tian Q, Zhang X, Yang A, Wang T, Zhang WH (2016) CIPK23 is involved in iron acquisition of Arabidopsis by affecting ferric chelate reductase activity. Plant Sci **246:** 70–79

Urzica EI, Casero D, Yamasaki H, Hsieh SI, Adler LN, Karpowicz SJ, Blaby-Haas CE, Clarke SG, Loo JA, Pellegrini M, et al (2012) Systems and trans-system level analysis identifies conserved iron deficiency responses in the plant lineage. Plant Cell **24:** 3921–3948

Vert G, Grotz N, Dédaldéchamp F, Gaymard F, Guerinot ML, Briat JF, Curie C (2002) IRT1, an Arabidopsis transporter essential for iron uptake from the soil and for plant growth. Plant Cell **14:** 1223–1233

Wang H, Tang J, Liu J, Hu J, Liu J, Chen Y, Cai Z, Wang X (2018) Abscisic acid signaling inhibits brassinosteroid signaling through dampening the dephosphorylation of BIN2 by ABI1 and ABI2. Mol Plant **11:** 315–325

Wedepohl KH (1995) The composition of the continental-crust. Geochim Cosmochim Acta **59:** 1217–1232